Czech Technical University in Prague

Faculty of Nuclear Sciences and Physical Engineering

Department of Solid State Engineering

Programme: Solid State Engineering

Generalized inverse problems in resonant ultrasound spectroscopy

MASTERS THESIS

Author: Bc. Juraj Olejňák

Supervisor: doc. Ing. Hanuš Seiner, Ph.D. DSc.

Year: 2021

I declare that I carried out this research study independently, and only with the cited sources, literature and other professional sources.

I understand that my work relates to the rights and obligations under the Act No. 121/2000 Coll., the Copyright Act, as amended, in particular the fact that the Czech Technical University in Prague has the right to conclude a license agreement on the use of this work as a school work pursuant to Section 60 paragraph 1 of the Copyright Act.

In Prague 3.5.2021 Bc. Juraj Olejňák

Acknowledgement

First of all, I would like to thank my supervisor doc. Ing. Hanuš Seiner, Ph.D. DSc. and consultant Ing. Petr Sedlák, Ph.D. for their willingness to help, valuable tips and immense patience. I would also like to thank Mgr. Michaela Janovská, Dr. and Ing. Lucie Bodnárová, Ph.D. for their help during sample preparation. Lastly, I would like to thank my family for their never ending support and trust.

Title: Generalized inverse problems in resonant ultrasound spectroscopy

Author: Bc. Juraj Olejňák

Department: Department of Solid State Engineering, Faculty of Nuclear Sciences and Physical Engineering, CTU in Prague

Supervisor: doc. Ing. Hanuš Seiner, Ph.D. DSc.

Abstract: The main aim of this thesis is to show the ability of the resonant ultrasound spectroscopy to precisely identify the anisotropy class, crystallographic orientations and dimensions of the sample, in addition to elastic coefficient determination. The reliability and robustness of our extended algorithm was tested on slightly perturbed synthetic data and on three differently oriented samples of FeSi single crystal. Precision of the results is discussed with respect to the number of resonances utilized during the procedure, and calculated crystallographic orientations are compared with the measurements obtained by Laue diffraction experiment. Our optimization procedure was then applied on room temperature measurements of 2 types of metastable β-Ti alloys with an increased amount of secondary phase particles after additional heat treatment. The aim was to observe potential change of the symmetry of the material after the phase transition. Our most important findings are summarized and discussed with respect to the character and morphology of the material's microstructure. Sample preparation and measurement of ultrasound spectra were conducted at the Department of Ultrasonic Methods, Institute of Thermomechanics of the Czech Academy of Sciences.

Keywords: resonant ultrasound spectroscopy, single crystals, titanium alloys, inverse procedure

Contents

1 Introduction

Elastic constants, like spring constants, can be determined by means of a static technique that measures a displacement as a linear response to a small applied force [1]. It was shown that even better method is to measure elastic vibrations of the given body by means of measuring the times of flights of sound pulses traveling through it. Simultaneously, more complex method called resonant ultrasound spectroscopy (RUS) which allows for determination of the elastic constants of the crystal was developed [1, 2, 3]. RUS is a process where one measures and evaluates the mechanical resonances or normal modes of a solid body. Since density, dimensions, and elastic moduli of the given body determine its mechanical resonances, the measurement of its resonance frequencies permits the determination of its elastic moduli [2]. However, determination of the elastic constants by RUS is a inverse problem so the experimentally obtained resonant frequencies cannot be directly recalculated into the elastic constants. Instead, an approximate spectrum is calculated from the known dimensions of the sample, its mass, and a set of 'guessed' elastic constants. The difference between computed and measured spectrum is caused by deviations in shape, homogeneity, and symmetry direction from those assumed in the computation [4]. A multidimensional minimization of the misfit between the measured and calculated spectra enables deducing all the elastic constants of the solid from a single frequency scan [5]. At first, such calculations were solvable only for spherical, non-crystaline materials but with increase in computational power and growing interest, especially from geophysics community, a different variety of crystalline material shapes can be used. Size and mass of the sample is limited only by the size of the aparatus, but usually samples not larger than a few milimeters are used. This technique is able to determine all 21 independent elastic constants when it is properly configured and complemented with pulse-echo measurement [6].

The measurement can be performed in contact-less regime and in low-pressure atmosphere, which reduces the damping of the vibrations and significantly improves the quality of the obtained spectra. During the data analysis, one must first solve the problem of calculating the natural frequencies in terms of elastic constants and sample shape and mass

(this is known as the forward problem), and then apply a nonlinear inversion algorithm to find the elastic constants from the measured natural frequencies (the inverse problem) [1].

This thesis aims to explore the possibility for the resonant ultrasound spectrosopy method to be used as a tool for the simultaneous identification of the anisotropy class, crystallographic orientation of the material and its elastic properties. Its methodology was extended by samples shape and orientation optimization algorithm. The reliability of our iterative optimization was tested on synthetic data containing small size and orientation perturbations and later on 3 differently oriented samples of the single crystal of a well-known material (silicon-doped Fe). Our algorithm was then applied on metastable β-Ti alloys containing particles of the low temperature coherent phase to obtain information about a possible change of the material symmetry during cubic to hexagonal diffusion driven phase transformation.

Notice that the ability of RUS to determine the crystallographic orientations has been already explored [7]. Here, however, our aim is to refine the orientations and the dimensions of the material accurately to obtain the best achievable fit and to discuss what is the highest number of observable resonances that can be involved in the inverse calculations.

2 Theory

2.1 Resonant ultrasound spectroscopy

As mentioned in the introduction, RUS is a technique used to measure elasticity of studied material. It relies on the measurement of the natural frequencies of the sample. These natural frequencies are dependent on the elasticity, shape and size of the sample when it is mechanically excited [8]. A basic theory concerned with RUS measurement and calculations will be explained in the following paragraphs.

2.1.1 Objective function minimization

Resonant ultrasound spectroscopy method of obtaining elastic coefficients contains an inverse procedure since the experimentally obtained resonant frequencies (ω^{exp}) cannot be directly recalculated into the elastic constants C_{ij} (Voigt notation). The inverse procedure of this method is done via minimization of the objective function:

$$\Delta\left(C_{ij}^{*}\right)=\sum_{n=1,\ldots,N}\left(\omega_{n}^{exp}-\omega_{n}^{calc}\left(C_{ij}^{*}\right)\right)^{2}, \tag{1}$$

where C_{ij}^{*} are iteratively refined guesses of our elastic constants, ω^{calc} are calculated resonant frequencies for our guesses, and N is the number of measured vibrational modes. A displacement fields of corresponding eigenmodes of vibrations $\mathbf{u}(\mathbf{x})$ are used to identify these vibrational modes.

According to Hamilton's principle, resonant frequencies ω and corresponding modal shapes $\mathbf{u}(\mathbf{x})$ can be obtained from the variational condition:

$$\frac{\delta}{\delta\mathbf{u}}\Lambda\left(\mathbf{u}(\mathbf{x}),\omega\right)=0, \tag{2}$$

where Λ is the Lagrangian energy of a harmonically vibrating body at the angular frequency ω, expressed as::

$$\Lambda\left(\mathbf{u}(\mathbf{x}),\omega\right)=\frac{1}{2}\int_{V}\left(\rho\omega^{2}u_{i}u_{i}-C_{ijkl}\frac{\partial u_{i}}{\partial x_{j}}\frac{\partial u_{k}}{\partial x_{l}}\right)\mathrm{d}\mathbf{x}, \tag{3}$$

where V is volume, ρ is density and C_{ijkl} is the tensor of elastic coefficients.

The variational condition (2) can be solved via functional discretization of modal shapes $\mathbf{u}(\mathbf{x})$. This process turns the equation into an eigenvalue problem:

$$0 = \nabla_\alpha \Lambda(\alpha) = \left(\omega^2 \mathbf{M} - \mathbf{K}\right) \alpha, \tag{4}$$

where $\mathbf{M}$ and $\mathbf{K}$ are symmetric and non-negative matrices and α is the vector of coefficients $\alpha_{[abc,i]}$ used in discretization:

$$u_i(\mathbf{x}) = \alpha_{[abc,i]} \psi_a(x_1) \psi_b(x_2) \psi_c(x_3), \tag{5}$$

where $\psi_m(x)$ are base functions. If the set of base functions $\psi_m(x)$ is orthogonal, the matrix M is diagonal, and the resulting eigenvalue problem is non-generalized [6].

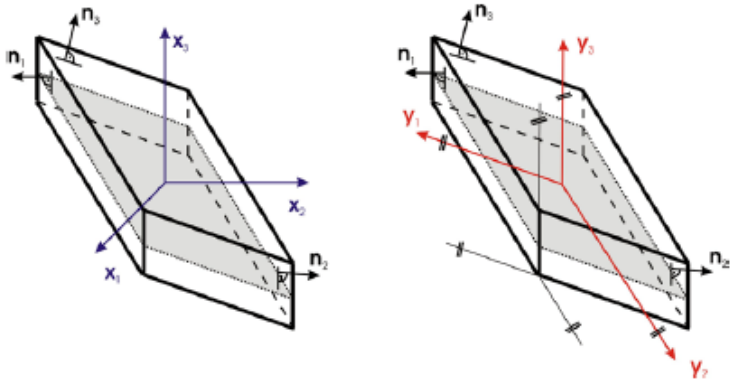

(a) Material coordinate system $\mathbf{X}$ (b) Edge coordinate system $\mathbf{Y}$

Figure 1: Geometry of general parallelepiped in different coordinate systems [3]

For homogeneous, anisotropic, nonrectangular parallelepiped samples an eigenmodes computation algorithm using Ritz method was developed [3].

If we have a anisotropic nonrectangular parallelepiped as shown in Figure 1 (its geometry is given by normals to its faces $\boldsymbol{n}_1$, $\boldsymbol{n}_2$, $\boldsymbol{n}_3$ and dimesions d_1, d_2, d_3). We search for the elastic tensor C_{ijkl} in the cartesian coordinate system $\mathbf{X} = \{\boldsymbol{x}_1, \boldsymbol{x}_2, \boldsymbol{x}_3\}$ which is usually connected with the symmetry directions of the examined material. On the other hand the nonorthogonal system $\mathbf{Y} = \{\boldsymbol{y}_1, \boldsymbol{y}_2, \boldsymbol{y}_3\}$ is connected with the edges of the studied sample (its base vectors are parallel to the edges of the sample).

We can consider linear transformation of vector coordinates in the basis $\mathbf{X}$ into coordinates in new basis $\mathbf{Y}$ as:

$$(\boldsymbol{p})_{\boldsymbol{Y}} = \mathbf{B}\,(\boldsymbol{p})_{\boldsymbol{X}}\,, \tag{6}$$

where $\mathbf{B}$ is regular transformation matrix. Using this substitution in the Lagrangian (3), we obtain:

$$\Lambda = \frac{1}{2}\int_{-\frac{d_1}{2}}^{+\frac{d_1}{2}}\int_{-\frac{d_2}{2}}^{+\frac{d_2}{2}}\int_{-\frac{d_3}{2}}^{+\frac{d_3}{2}}\left[\frac{\rho}{\xi}\omega^2 u_i^2(y) - T_{ijkl}\frac{\partial u_i}{\partial y_j}(y)\frac{\partial u_k}{\partial y_l}(y)\right]\mathrm{d}y_1\mathrm{d}y_2\mathrm{d}y_3, \tag{7}$$

where $\xi = \det \mathbf{B}$ is the Jacobian of the transformation and

$$T_{ijkl} = \frac{1}{\xi}C_{ipko}\boldsymbol{B}_{jp}\boldsymbol{B}_{lo}, \tag{8}$$

is the four-dimensional array that relates the elasticity of the material with the sample geometry given by the product $\boldsymbol{B}_{jp}\boldsymbol{B}_{lo}$ [3].

More details and role of this array in our geometry and shape optimization algorithm will be discussed in paragraph 2.14.

2.1.2 Iterative matching of the resonant modes

We are able to evaluate objective function (1) for any guess of the elastic constants C_{ij}^*. The projection of the surface displacement field for each found eigenmode onto the normal of the faces of the sample enables a direct comparison between experimental and calculated modal shapes (see [9, 6]). The correct matching of experimental and calculated modes must be ensured. This is a source of many errors in classical RUS measurements, where the vibrations are detected only at a single position of the sample [10], and the association of the modes is performed according to the simple ordering of the calculated and measured modes. This problem could be solved by the employment of scanning laser interferometer that provides the accurate shape of each resonant mode [11]. There is a dependence of the set of the modal shapes on the elastic constants which means that for a initial guess of the elastic constants there is a limited set of modes that can be used in the inverse procedure. All the other experimentally obtained modes have not yet received

their calculated counterpart [6]. This problem is resolved by iterative approach which means that the calculated elastic constants in the first step are then used as initial guesses for the next iteration, and since the guesses are optimized, an extension of the set of modes is obtained, increasing the number of modes which can be successfully identified. The whole procedure is repeated a few times, until a sufficient number of experimentally obtained resonant modes is well identified and successfully paired with the calculated ones. The experimental and calculated modal shapes are subsequently matched together according to visual appearance. The procedure for the determination of elastic constants is schematically shown in Figure 2.

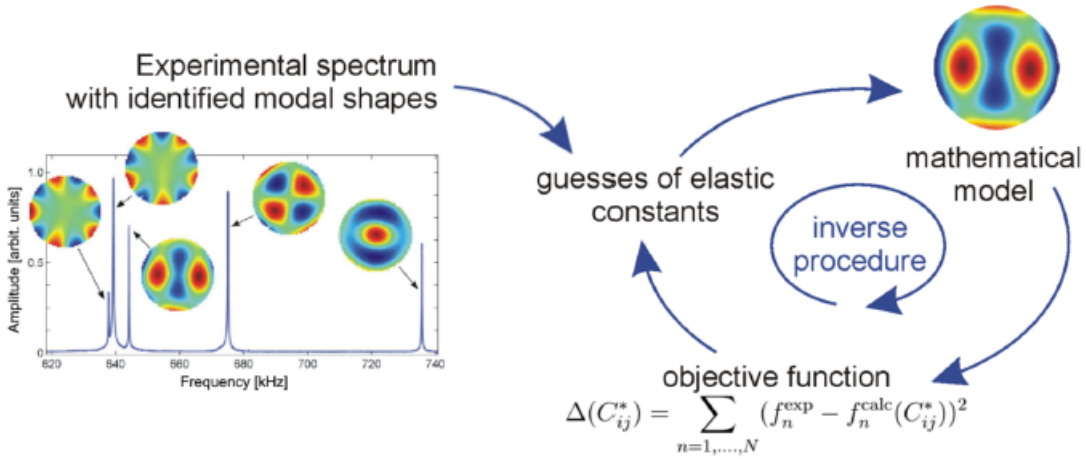

Figure 2: Procedure of determination of elastic constants from the RUS measurement [10].

2.1.3 RUS sensitivity

Elastic coefficients obtained from RUS are a result of an inverse problem solution, i.e., they are achieved by minimizing the objective function (1), which is the difference between the measured resonant frequencies and those calculated from iteratively improved guesses. The number of resonant frequencies utilized for the inverse procedure may vary from less than ten to few hundred, depending on the vibration damping in the given material, group of symmetry we are using in our calculations (how many elastic constants we are seeking) and overall quality of the experimental data[12].

Measurements based on RUS are especially suitable for the determination of the softest shear elastic coefficient of strongly anisotropic cubic materials, since the lowest resonant modes of such materials are not very sensitive to small deviations in the orientation of the crystal used in experiment. These small errors can arise either from incorrect cutting of the sample during preparation or from experimental error during measurement of the crystallographic orientation by the Laue/EBSD method or their combination, which is usually the case [12].

To ensure a well defined minimum of the objective function (1) there is a need to determine which parts of the elastic tensor can be reliably identified in each step of the iteration and which cannot. An approach based on perturbation theory is used [6].

The derivative of the i-th resonant frequency with respect to a given set of independent elastic constant c_P can be expressed as:

$$\frac{\partial \omega_i}{\partial c_P} = \frac{1}{2}\frac{1}{\omega_i^{exp}}\alpha_{(i)}^T \frac{\partial \mathrm{K}}{\partial c_P}\alpha_{(i)}, \tag{9}$$

where $\alpha_{(i)}$ is the eigenvector corresponding to the i-th mode. $\frac{\partial \mathrm{K}}{\partial c_P}$ is independent on the values of the elastic constants and thus can be calculated before the start of the minimization. We then define a sensitivity matrix $\mathbf{S}$:

$$\mathrm{S} = 2 \begin{bmatrix} \frac{\partial \omega_1}{\partial c_1} & \vdots & \frac{\partial \omega_k}{\partial c_1} \\ \vdots & \ddots & \vdots \\ \frac{\partial \omega_1}{\partial c_Q} & \vdots & \frac{\partial \omega_k}{\partial c_Q} \end{bmatrix} . \begin{bmatrix} \frac{\partial \omega_1}{\partial c_1} & \cdots & \frac{\partial \omega_1}{\partial c_Q} \\ \vdots & \ddots & \vdots \\ \frac{\partial \omega_k}{\partial c_1} & \cdots & \frac{\partial \omega_k}{\partial c_Q} \end{bmatrix}, \tag{10}$$

which is approximation of the Hessian matrix of the objective function in the minimum. If the matrix $\mathbf{S}$ is diagonal, sensitivities of the spectrum with respect to individual elastic constants are uncorrelated, and the diagonal components $\boldsymbol{S}_{PP}$ define their values. If the matrix $\mathbf{S}$ is not diagonal, the sensitivities are mutually correlated and we need to apply eigenvalue decomposition to diagonalize the $\mathbf{S}$ [6]. We can choose such eigenvectors that they form an orthogonal basis ($\mathbf{G}^{-1} = \mathbf{G}^T$) and the eigenvalues are real, non-negative (thanks to matrix $\mathbf{S}$ being symmetric and positively semi-definite). We are then able to always find a set of linear combinations $c_P^{(G)} = \sum c_R \mathbf{G}_{PR}$ where the diagonal terms $\lambda_P = (\boldsymbol{GSG}^{-1})_{PP}$ are above some chosen threshold value. We then allow only those sets

of combinations to participate in the inverse procedure. The values of λ_P as well as the number of linear combinations $c_P^{(G)} = \sum c_R \mathbf{G}_{PR}$ increase with successful elastic constants refinement and with increasing number of the modes involved in the inversion. However, some of the linear combinations $c_P^{(G)}$ may remain indeterminable from the RUS spectrum even if all available experimental resonant frequencies are involved and all corresponding modal shapes are indubitably identified [6]. This happens because RUS works with the lowest fraction of the spectrum and that is why is RUS measurement usually complemented with pulse-echo measurement.

The experimental error of the P-th elastic constant can be estimated as:

$$\Delta C_R = \sqrt{\sum_{P=1}^{Q} \left(\mathbf{G}_{RP}^{-1}\right)^2 \frac{2\Delta\left(C_1^{opt}, ..., C_Q^{opt}\right)}{N\lambda_P}}, \tag{11}$$

where Δ is our objective function, $\mathbf{G}_{RP}^{-1}$ is the R-th normalized eigenvector of the Hessian matrix $\frac{\partial^2 \Delta}{\partial C_I \partial C_J}$, λ_P the corresponding eigenvalue, Q is a number of independent elastic constants, N is the number of resonant modes involved in the inverse procedure, $C_1^{opt}, ..., C_Q^{opt}$ is an optimal set of elastic constants gained by minimization of the objective function (1) [13].

A more detailed description of RUS calculations, especially of error estimation is available in [6].

2.1.4 Geometry and shape optimization

As mentioned in paragraph 2.1.1, the combined effect of materials elasticity and sample geometry on the resonant spectrum is defined through four-dimensional symmetrical array T_{ijkl} ($T_{ijkl} = T_{klij}$). When this array is used, it keeps the displacement vector $\mathbf{u}$ in the original coordinate system $\mathbf{X}$ (even if it is a function of the nonorthogonal coordinates $\mathbf{Y}$) [3].

The eigenstates (stationary points) of the Lagrangian energy (7) are sought using expansion into polynomial basis so that the calculation is turned into the eigenvalue problem

$$\left(\omega^2 \mathrm{E}_{[abc,i],[def,j]} - \mathbf{\Gamma}_{[abc,i],[def,j]}\right) \alpha_{[abc,i]} = 0, \tag{12}$$

where

$$\mathrm{E}_{[abc,i],[def,j]} = \delta_{ij}\delta_{ad}\delta_{be}\delta_{cf}, \tag{13}$$

and

$$\mathbf{\Gamma}_{[abc,i],[def,j]} = \frac{\xi}{\rho}\frac{8}{d_1 d_2 d_3} T_{ijkl} \int_{-\frac{d_1}{2}}^{+\frac{d_1}{2}} \int_{-\frac{d_2}{2}}^{+\frac{d_2}{2}} \int_{-\frac{d_3}{2}}^{+\frac{d_3}{2}} \frac{\partial \psi_{abc}}{\partial y_k} \frac{\partial \psi_{def}}{\partial y_l} \mathrm{dy}_1 \mathrm{dy}_2 \mathrm{dy}_3. \tag{14}$$

Here, ψ are base functions of the Ritz method in the form

$$\psi_{abc} = P_a\left(\frac{2y_1}{d_1}\right) P_b\left(\frac{2y_2}{d_2}\right) P_c\left(\frac{2y_3}{d_3}\right), \tag{15}$$

where a, b, c = 0, 1, 2, 3, ... , a + b + c $\leq$ N, and $P_n(y)$ is the normalized Legendre polynomial of degree n

$$P_n(y) = \frac{\sqrt{(2n+1)/2}}{2^n n!}\left[\frac{d^n}{dy^n}\left(y^2-1\right)^n\right], \tag{16}$$

The accuracy of the solution depends on the maximum degree of the Legendre polynomial N. Precision is increased with increasing N but so is the computational time [3]. Convergence of the calculation with respect to the N can be checked. By combining equations above we can take a closer look at the matrix Γ

$$\mathbf{\Gamma}_{[abc,i],[def,j]} = \frac{8}{d_k d_l}\frac{1}{\rho} C_{ipjo} \boldsymbol{B}_{kp} \boldsymbol{B}_{lo} D_{[kl,abc,def]}, \tag{17}$$

where $D_{[kl,abc,def]}$ are constants obtained from the integration of the Legendre polynomials and their derivatives and are independent of particular sample dimensions d_i, thus can be calculated in advance. $\boldsymbol{B}_{kp}\boldsymbol{B}_{lo}$ represents the orientation of the sample (with respect to the principal axes of the material) and C_{ipjo} is the elasticity of the studied material. We can rewrite this expression, which incorporates all of the above mentioned variables

$$\mathbf{\Gamma}_{[abc,i],[def,j]} = \widetilde{T}_{ijkl} D_{[kl,abc,def]}, \tag{18}$$

where "quasi-tensor" $\widetilde{T}_{ijkl} = \frac{8}{\rho d_j d_l} T_{ikjl}$. This way, $\widetilde{T}_{ijkl}$ can be now subject to minimization of the objective function (1), instead of C_{ijkl}. In other words, up until now the process of obtaining elastic coefficients consisted of minimization of the objective function (1), where our calculated frequencies ω_n^{calc} were functions of the sought elastic coefficients C_{ijkl}, and known density of the material ρ and known geometry of the sample ($\omega_n^{calc} = \omega_n^{calc}(C_{ijkl}, \rho, \text{geometry})$). Our extension of this algorithm leads to the same minimization process but formally changes the dependence of the ω_n^{calc} from C_{ijkl} and geometry to sought $\widetilde{T}_{ijkl}$ and known density ρ, ($(\omega_n^{calc} = \omega_n^{calc}\left(\widetilde{T}_{ijkl}, \rho\right)$). This enables small changes in the geometry of the material and thus allows us to not only successfully find elastic constants C_{ijkl} but also to refine samples dimensions and crystallographic orientation. To obtain suitable precision in establishing samples geometry (error $\leq 1\%$) a very high number of successfully matched modal shapes and their corresponding frequencies must be ensured. The amount of obtainable independent elastic coefficients rose from 21 (in case of C_{ijkl}) to 45 with the implementation of the $\widetilde{T}_{ijkl}$. The inversion procedure of $\widetilde{T}_{ijkl}$ remains the same as of the C_{ijkl}.

Moreover, a simplification of the procedure can be utilized. Rather than evaluating data using full triclinic symmetry and minimizing the objective function (1) with respect to $\widetilde{T}_{ijkl}$, which means fitting the elasticity and geometry based on the result, we can assume some symmetry (cubic in our case), construct $\widetilde{T}_{ijkl}$ with addition of parameters for geometry and shape refinement, and optimize the created cubic composite function ($\widetilde{T}_{ijkl}^{cubic}$). This composite function contains 11 variables: 3 for independent elastic coefficients in cubic symmetry, 2 for dimensions (one dimension needs to be fixed due to scaling problem) and 6 for orientation (2 for each direction). The architecture of the inversion procedure still remains the same.

2.2 Time-of-flight methods

Since RUS carries mainly information about shear elastic coefficients (RUS does not allow accurate determination of c_{11} coefficient even when high number of modes is successfully matched and crystallographic orientation is accurately known) another methods for elastic constants determination must be used to complement more complex RUS measurement.

Time-of-flight methods (TOF) belong to the most used and simplest methods for determination of elastic coefficient of solids using ultrasonic waves. The ultrasonic transducer used in TOF measurement is typically in contact with one of the faces of the sample. This transducer emits planar waves propagating in direction perpendicular to the face, which are then recorded at either the opposite face (the through-transmission arrangement) while using another transducer, or by the same transducer after reflecting from the opposite face (the pulse-echo arrangement) [12]. For the experiment reported in this thesis, we have chosen the approach base on the pulse-echo arrangement.

By measuring times-of-flight of these planar ultrasonic waves between two parallel surfaces and from the thickness of the sample, we can calculate velocities of the waves in specific directions. These velocities contain information about the elastic properties of the studied specimen. Planar waves in generally anisotropic material can propagate only at phase velocities v_φ (in any direction $\mathbf{n}$) that [9]

$$\det\left(C_{ijkl}n_jn_l - \rho v_\varphi^2\delta_{ik}\right) = 0, \tag{19}$$

where ρ is the density of the material and C_{ijkl} are elastic coefficients. Expression ρv_φ^2 is eigenvalue of Christoffel matrix $\Gamma_{ik} = C_{ijkl}n_jn_l$. In general, we get three different velocities for each direction. The values of the fastest (longitudinal) velocities are later used as input for elastic coefficient calculations from data obtained via resonant ultrasound spectroscopy measurements.

3 Experimental setup

3.1 Pulse-echo

Pulse-echo measurement is schematically shown in Figure 3. The same probe is used for the generation of the pulse and also for its detection when it returns reflected from the opposite side of the sample. For better acoustic coupling between the probe and the specimen, a small drop of propylene glycol is used. Times-of-flight for each specimen and each main direction are measured using an oscilloscope. Velocities that are needed during RUS data evaluation are calculated using the simple equation:

$$v = \frac{2T}{t}, \tag{20}$$

where T is the dimension of the sample in the wave propagation direction and t are times-of-flight. Factor 2 is used because the wave is detected after it travels through specimen twice.

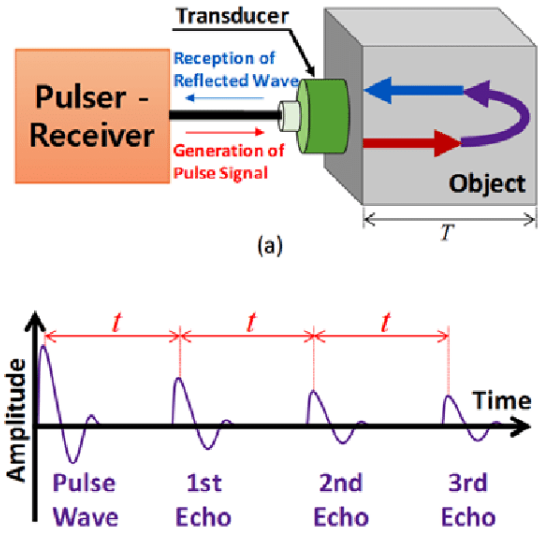

Figure 3: Schematic of pulse echo measurement [14].

3.2 Resonant ultrasound spectroscopy

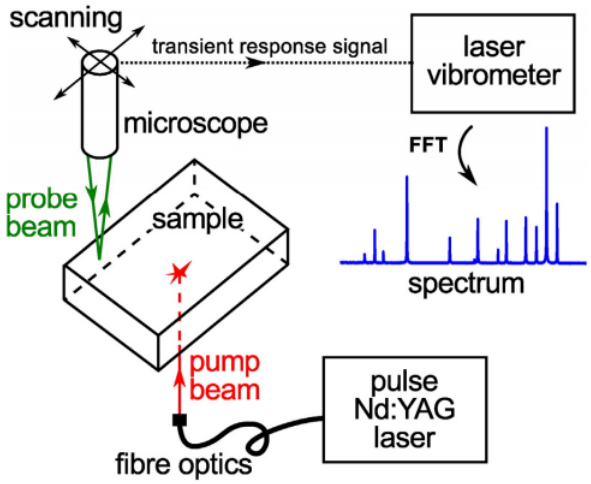

Figure 4: Schematic of RUS measurement [15].

Schematic of RUS measurement is shown in Figure 4. The device and software for calculations were developed at Department of Ultrasonic Methods, Institute of Thermomechanics of Czech Academy of Science. The sample is freely laid in a vacuum chamber onto roughly machined copper underlay to ensure the best approximation of free elastic vibrations. This small mechanical contact between the sample and the chamber results in minimal energy transmissions. Chamber was evacuated and filled with approximately 20 mbar of nitrogen to ensure temperature control of the sample. The temperature of the chamber is controlled via Peltier modules located in the vicinity of the sample. Temperature measurement was provided by small Pt100 resistance thermometer embedded in the copper underlay directly under the sample. After a long stabilization time, the temperature measured on the thermometer was assumed to be equal to the temperature of the sample. Vibrations of the sample are generated by short (8 ns) pulses from infrared Nd:YAG laser ($\lambda = 1,064\,\mu$m) which were driven to the chamber by an optical fibre and focused onto the lower surface of the sample by high energy fiber focuser. Samples response to these pulses was scanned from above through a small fused silica window by scanning laser vibrometer. Different elements of the RUS aparatus are shown in Figure 5. The surface was scanned in regular mesh ranging from 20 x 20 to 50 x 50 points, depending on the precision and quality of the measurement we want to obtain. A more detailed description is available in [6].

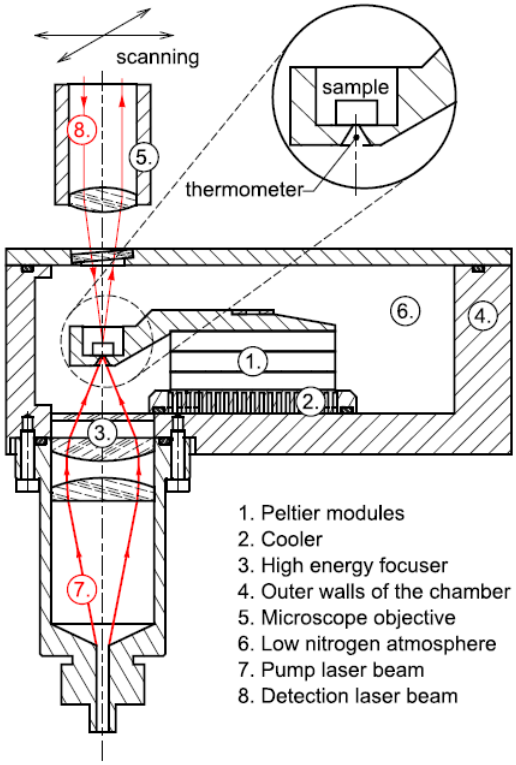

Figure 5: The instrumentation of the RUS set-up used for the experiments [6].

4 Experimental material

4.1 Synthetic data

We used synthetic data for reliability testing of our new extended algorithm. We created MatLab script which applied small perturbation to our data, and lead to a deviation of a few degrees in crystallographic orientation and a few μm in dimensions. The perturbation to the orientation was accomplished by taking the normal vectors of the faces perpendicular to the considered one, multiplying said vectors by a small number randomly generated from set interval, and adding them to the original normal vector of the considered face. The perturbation to the size of the sample consisted only of multiplication of the original dimensions by a small randomly generated number close to 1. Only two of the three dimensions were perturbed to avoid scaling problem. We then generated around 200 resonant peaks and their corresponding modal shapes for set of different crystallographic orientations for the cubic symmetry.

Afterwards, we treated the synthetic data as experimental inputs for the inverse procedure. We used the knowledge of the symmetry of the data and ran the minimization procedure of the composite function (described in paragraph 2.1.4.) to verify if each test converged to the same elastic constants, and to identify perturbed geometry and orientation correctly. For some of the tests we also changed the amount of perturbation applied on the data to find a limit where it is no longer possible to even successfully match few "measured" and computed frequencies and modal shapes.

Overall around 20 different sets of crystallographic planes ranging from more simple low-index to more general planes were created and tested. The notation of crystallographic planes is shown in Figure 6 and few examples of generated data are shown in Table 1. Crystallographic orientation of generated planes is given by normals to its faces (h,k,l).

For the synthetic data, we used density $\rho = 6.45$ g/cm^3 and initial guesses of the elastic coefficients $c_{11} = 170$ GPa, $c_{12} = 120$ GPa, $c_{44} = 60$ GPa in our optimization procedure. Legendre polynomials of 20th order were utilized during the inversion calculations.

The unperturbed sets of crystallographic orientations are shown in the third column of Table 1. The unperturbed dimensions were: $d_{red} = 3$ mm, $d_{blue} = 2.5$ mm, $d_{green} = 2$ mm.

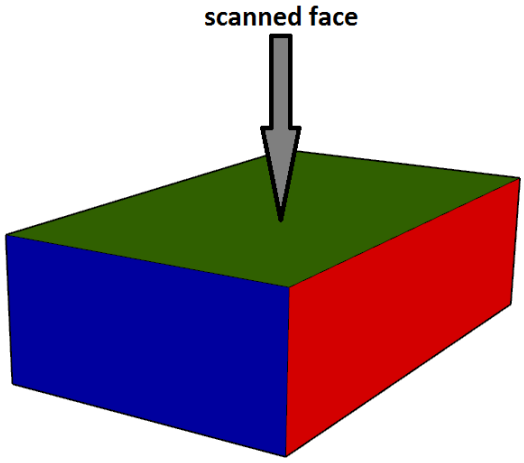

Figure 6: Notation for generated crystallographic planes

Table 1: Examples of generated data

Test no.	Face	Unperturbed planes (h, k, l)	Perturbed planes (h, k, l)	Perturbed dimensions [mm]
Test 3	red	(1, 1, 1)	(0.55, 0.60, 0.57)	3
	blue	(-1, 1, 0)	(-0.69, 0.73, 0.03)	2.494
	green	(1, 1, -2)	(0.40, 0.39, -0.82)	2.009
Test 16	red	(2, 2, 1)	(0.65, 0,70, 0.30)	3
	blue	(-1, 2, 0)	(-0.46, 0.89, -0.05)	2.495
	green	(1, 1, -2)	(0.44, 0.38, -0.81)	2.001
Test 23	red	(3, 1, 1)	(0.90, 0.33, 0.27)	3
	blue	(-1, 3, 0)	(-0.32, 0.95, -0.04)	2.495
	green	(3, 1, -3)	(0.71, 0.19, -0.68)	2.001

For the inverse calculation, we treated the synthetic data as experimental spectra for samples with the unperturbed orientations and dimensions obtained from the measurements. These unperturbed orientations and dimensions served as initial values during optimization procedure.

4.2 FeSi single crystal

For experimental verification of our minimization procedure we chose a well-known cubic material - single crystal of Fe containing around 3 wt.% of Si. Such a small amount of Si significantly improves corrosion resistance of Fe single crystal and does not have any major influence on the elastic constants C_{ij} [16].[1]

During our pulse-echo measurement we confirmed expected anisotropy of this alloy.

To quantify the anisotropy of the cubic material a so-called Zener anisotropy ratio can be used

$$A = \frac{2c_{44}}{c_{11} - c_{12}}, \tag{21}$$

for single crystals of pure metals this ratio is typically between 1 and 3 [12].

We cut 3 parallelepiped samples with different orientations, as outlined in Figure 7. First one (FeSi1) was cut according to the crystallographic orientation established by Laue measurement. Assumed orientation for first sample is show in Table 2 (notation of the faces in Figure 6). Second one (FeSi2) was cut under the angle $\theta < 45°$ which meant that the orientation of the scanned face remained the same as for the first sample and the orientation of the both side faces became unknown. The third sample (FeSi3) was cut under the same angle θ as the sample 2 but the scanned face was deliberately inclined by polishing by a small angle ψ, such that all 3 faces had unknown orientation. Difference in orientation of the samples can be seen in Figure 7. Dark axes denote coordinate system of unrotated sample FeSi1, while the light axes denote new coordinate systems of rotated samples FeSi2 and FeSi3.

[1] We will further refer to this material as FeSi, although the amount of Si is very small. With increasing amount of Si, iron and silicon form four compounds, $FeSi_2$, Fe_5Si_3, FeSi, $\alpha - FeSi_2$ and $\beta - FeSi_2$ [17]. Among them, only FeSi and the low temperature modification of $FeSi_2$, the beta-phase, are thermodynamically stable at room temperature [18]. While $\beta - FeSi_2$ is orthorhombic FeSi single crystal crystalizes in cubic symmetry and has semiconducting properties which exhibits band feromagnetism [19]. Single crystals of FeSi are usually grown from mixture of powder of corresponding elements using Czochralski or Bridgman technique.

Assumed crystallographic orientations shown in Table 2 were used as a input parameters at the start of the inverese calculations. We used our new tested geometry and shape optimization algorithm to successfully determine elastic coefficients and refine crystallographic orientations and dimensions of each sample. We also quantified anisotropy of the material with the established anisotropy ratio A.

Table 2: Assumed crystallographic orientation of the sample FeSi1

Sample	Face	Planes (h, k, l)
FeSi1	red	(0, 0, -1)
	blue	(1, -1, 0)
	green	(1, 1, 0)

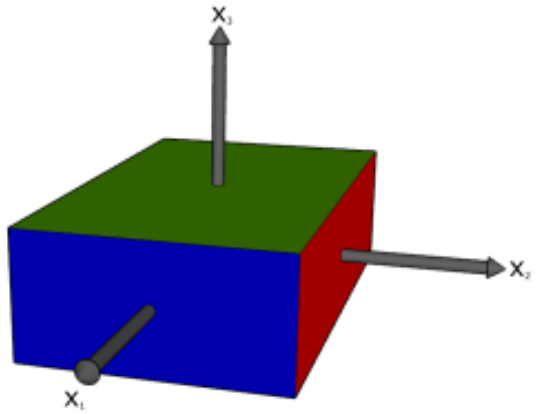

(a) Sample FeSi1

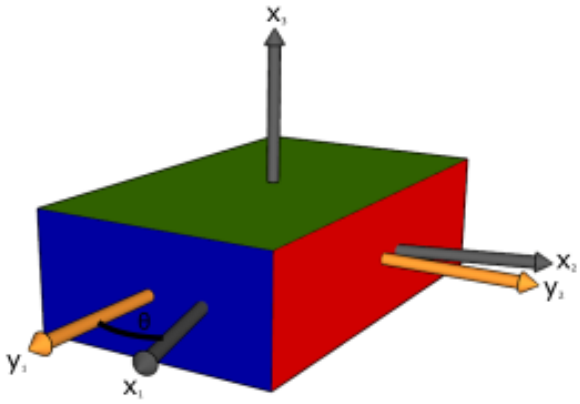

(b) Sample FeSi2

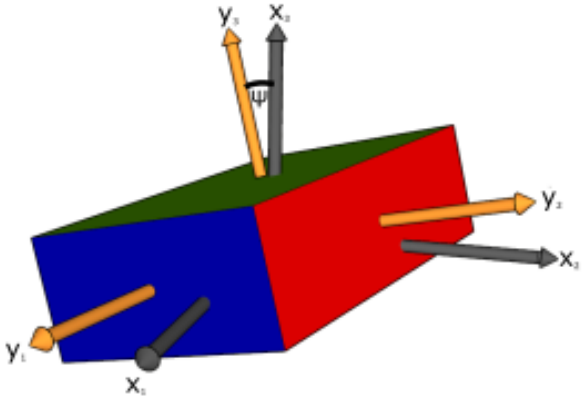

(c) Sample FeSi3

Figure 7: Changes in orientation of the FeSi samples

4.3 Metastable beta-Ti alloys

After testing of the minimization procedure on synthetic data and known material, we focused on the characterization of the single crystals of metastable β-titanium alloys. We chose single crystals of two alloys containing particles of the low temperature coherent phase, with the aim to confirm the tendency of such alloys to remain in the cubic symmetry even after the growth of their second-phase particles.

4.3.1 Theoretical background of Ti alloys

Titanium alloys are divided into four groups (Figure 8) based on the amount of alloying elements: α-titanium alloys, $\alpha + \beta$-titanium alloys, metastable β-titanium alloys, and stable β-titanium alloys.

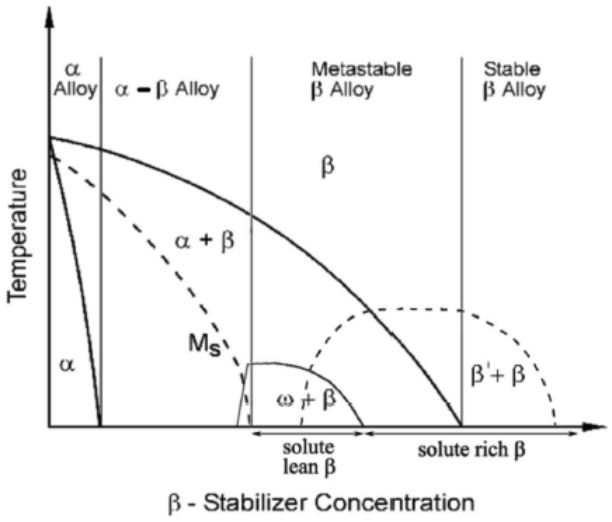

Figure 8: Schematic phase diagram of Titanium alloys [20].

α alloys contain mostly neutral or α-stabilizing elements but may contain small amounts of β-stabilizers. Because β-stabilizers can be present only in such small quantities, a metastable structure cannot be created. With an increased amount of β-stabilizers, which have the temperature of martensite transformation start (M_S) above room temperature, we move to the $\alpha+\beta$ alloys region. These two-phase alloys are stable at room temperature and belong to the most widely used alloys (Ti-6Al-4V and Ti-6Al-7Nb alloys). The main

advantages of these alloys are good toughness, high strength, and great corrosion resistance. Further increase of β-stabilizing elements leads to a decrease in M_S just below room temperature, and the β phase is no longer transformed upon quenching. These alloys belong to the metastable β-titanium alloys group, and they can still contain some amount of secondary α particles at equilibrium. Their characteristics are similar to $\alpha + \beta$ alloys with the addition of low elastic modulus, good fatigue resistance, and formability. They are the most versatile titanium alloys even though they have higher density and higher cost in comparison with $\alpha + \beta$ alloys and can even be used in medicine due to their biocompatibility. With an even more increased amount of β-stabilizing elements, these alloys become stable at room temperature – hence the name stable β-titanium alloys. These alloys can no longer be hardened via precipitation and therefore have no commercial application due to poor mechanical properties. Therefore, the term β-titanium alloys usually correspond to metastable β-titanium alloys [21, 10].

Phases that correspond to the local but not global minimum of Gibbs free energy (G) are called metastable. Titanium alloys may contain some of the metastable phases which can improve its properties. One of the most studied metastable phases is hexagonal ω-phase. It is formed by collapsing two neighbouring planes $\{111\}_\beta$ as each third plane stays fixed [22]. ω-phase precipitates are coherent with parent β-matrix and β-phase plain (111) corresponds to (0001) plane in ω-phase [23]. According to [24] we are able to distinguish between two types of ω-phase. The first phase, called athermal (ω_{ath}), is formed upon quenching from β phase. This phase formation is diffusionless and transformation is reversible. The second phase, called isothermal (ω_{iso}), can be developed during ageing in the temperature range of approximately 100 – 500 °C. Growth of ω_{iso}particles from ω_{ath} which remained after heating is controlled by diffusion and accompanied by a shift of the lattice parameter of the β-phase [21]. ω-phase can also form in samples that are subjected to severe deformations (equal channel pressing or high pressure torsion [25, 26]).

4.3.2 LCB and Ti-15Mo alloys

We chose 9 metastable beta-Ti alloys - 4 samples of LCB alloy (6.8 wt.% Mo, 4.5 wt.% F, 1.5 wt.% Al) and 5 samples of Ti-15Mo alloy (15 wt.% Mo) which underwent heat treatment (HT) under different temperatures, times and pressures. Their respective information about the heat treatment is shown in Table 3. The ageing temperature of 300° C in most cases was chosen to achieve a very high volume fraction of well developed ω_{iso} phase particles without any significant α phase precipitation [27].

As mentioned above, our main focus is to establish to what amount the material remains macroscopically cubic and detect the level of randomness of secondary coherent phases.

Table 3: Basic information about HT of the metastable beta-Ti alloy samples

Name	Temperature [°C]	Time [h]	Note
LCB_m8h1	300	8	
LCB_mono8h2	300	8	
LCB_mono128h2	300	128	
LCB_ST2_tc750	750	-	heat cycle up to 750 °C
Ti15Mo_AB_tc750	750	-	heat cycle up to 750 °C
Ti15Mo_L	300	4	
Ti15Mo_R_po400	400	16	
Ti15Mo_V	300	6	HT under pressure of 800 MPa
Ti15Mo_W	300	6	HT under pressure of 1000 MPa

The transmission electron microscopy (TEM) observation confirmed that all of the aged samples were composed of cubic matrix of β phase with nano-sized particles of ω phase. Occurrence of α phase was excluded for all samples aged below 500°C [13, 27]. Measurements of the volume fractions for the LCB alloys by x-ray diffraction were reported in [28] , while more accurate estimates were obtained from RUS measurement[27]. Measurements for the Ti15Mo performed by RUS are reported in [13].

Assumed volume fractions (λ) of the ω phase:

- Aged samples of the LCB alloy: $\lambda \approx 0,50$
- Aged samples of the Ti15Mo alloy: $\lambda \approx 0,62$
- Samples of both alloy subjected to heating cycles to 750°C contained an unknown amount of the α phase, and possibly also some residual ω phase.

5 Results and discussion

5.1 Tests on synthetic data

Due to the amount of data the result will be discussed with respect to two of the performed tests only. As mentioned in paragraph 4.1 we created synthetic data containing around 200 resonant peaks and their corresponding modal shapes. Spectrum showing all the generated resonant peaks can be seen in Figure 9. The evolution of the selected resonant modes (modal shapes and resonant frequencies) with multiple iterations and with increasing number of matched resonant modes utilized in the minimization procedure can be seen in Figures 10 - 12. During the calculations, algorithm utilized 30 matched resonant modes for the first iteration, 60 for the second iteration, 90 for the third and 120 for the last iteration.

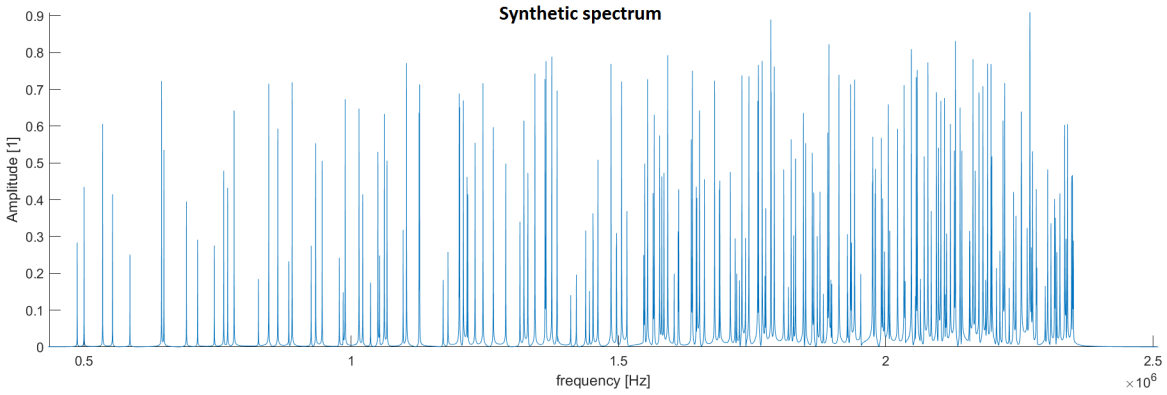

Figure 9: Example of generated resonant spectrum

First of the examples is Test 3, containing low-index planes (1, 1, 1); (-1, 1, 0); (1, 1, -2). We started the calculations using non-perturbed orientations (Table 1) as input parameter and optimized the structure using our generalized optimization procedure, constraining the symmetry of elasticity to cubic. To confirm the optimization was successful, we compare the perturbed orientations and dimensions used for the generation of the synthetic spectra with the ones refined during our cubic inversion. Table 4 shows the values of the refined and as-generated (perturbed) orientations and dimensions. The notation of crystallographic planes is shown in Figure 6. Crystallographic orientation of generated planes is given by normals to its faces (h,k,l).

Table 4: Perturbed and refined orientations and dimensions

Face	Perturbed planes (h,k,l)	Refined planes (h,k,l)	Perturbed dimensions [mm]	Refined dimensions [mm]
red	(0.55, 0.60, 0.57)	(0.55, 0.60, 0.57)	3	3
blue	(-0.69, 0.73, 0.03)	(-0.69, 0.73, 0.03)	2.502	2.502
green	(0.40, 0.39, -0.82)	(0.40, 0.39, -0.82)	2.993	2,.993

By comparing the results of the perturbed and refined orientations and dimensions, we can see that our cubic inversion procedure was very successful and managed to refine the orientations and dimensions precisely to their perturbed values used in generation of the specrum. Misfit between perturbed orientations and the ones used as an input in inverse calculations (Table 1) is 1.1° for the scanned face (green), 2.1° for the red and 2.3° for the blue face.

Furthermore, we have managed to successfully refine the orientations and dimensions while the elastic coefficients converged to the initial guesses with high precision:

$$c_{11} = (169.99 \pm 1.1)\,\mathrm{GPa}$$

$$c_{12} = (120.02 \pm 0.94)\,\mathrm{GPa}$$

$$c_{44} = (59.99 \pm 0.39)\,\mathrm{GPa}$$

Figures 10 - 12, show that with increasing number of performed iterations and successfully matched resonant modes the parameter Δf, characterizing the difference between synthetic resonant mode frequency and its calculated counterpart, is decreasing drastically. Since the perturbation applied on the data was very small, we have managed to successfully optimize the data already after the first two iterations. The third and last iterations were performed to minimize the parameter Δf as much as possible. More iterations were not necessary, since desired precision was successfully achieved.

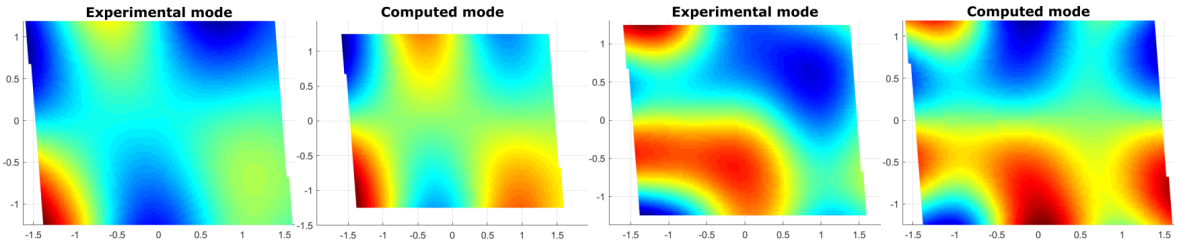

(a) Mode no. 21 ($\Delta f = 1{,}36$ kHz) (b) Mode no. 40 ($\Delta f = 9{,}76$ kHz)

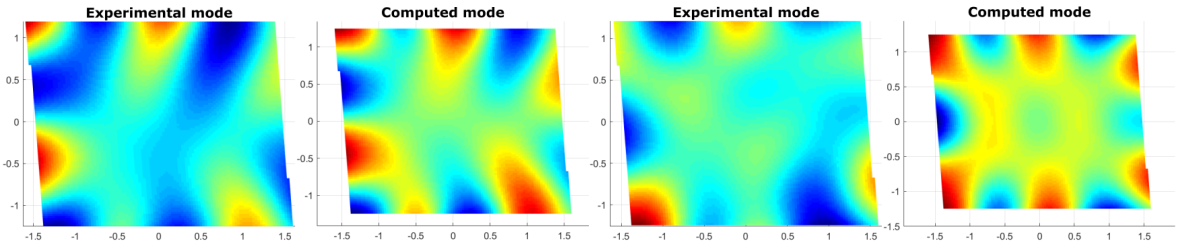

(c) Mode no. 61 ($\Delta f = 5{,}26$ kHz) (d) Mode no. 79 ($\Delta f = 8{,}57$ kHz)

Figure 10: Comparison of synthetic and calculated resonant modes at the start of the inversion

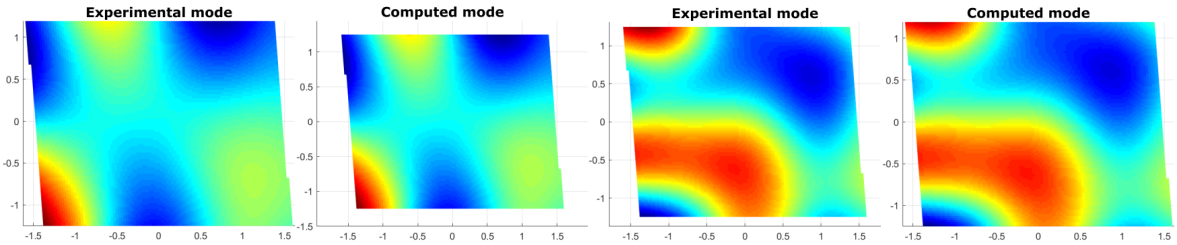

(a) Mode no. 21 ($\Delta f = 0{,}05$ kHz) (b) Mode no. 40 ($\Delta f = 0{,}12$ kHz)

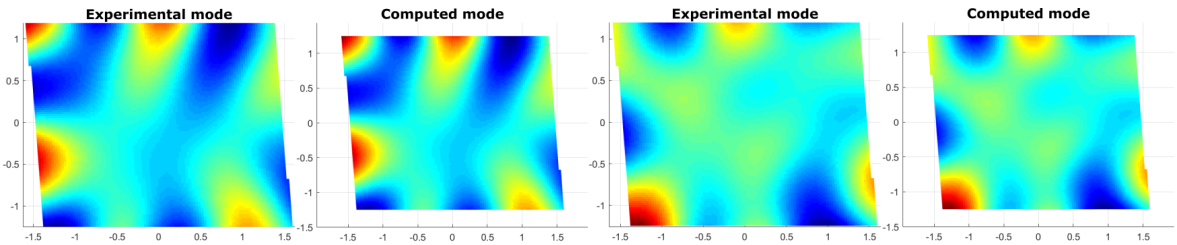

(c) Mode no. 61 ($\Delta f = 0{,}09$ kHz) (d) Mode no. 79 ($\Delta f = 0{,}14$ kHz)

Figure 11: Comparison of synthetic and calculated resonant modes after the second iteration

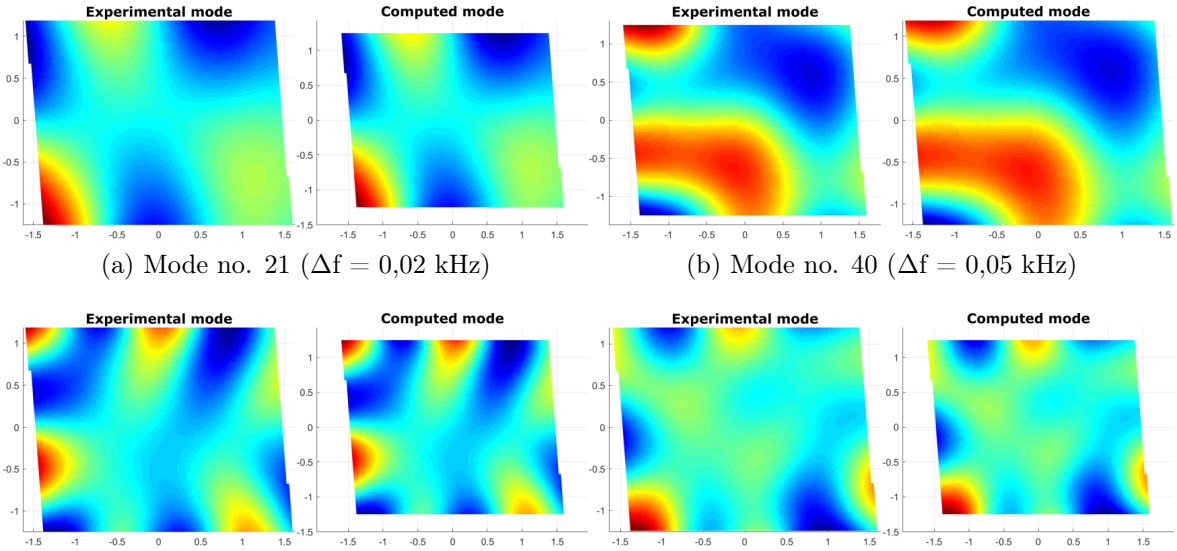

(a) Mode no. 21 (Δf = 0,02 kHz) (b) Mode no. 40 (Δf = 0,05 kHz)

(c) Mode no. 61 (Δf = 0,01 kHz) (d) Mode no. 79 (Δf = 0,11 kHz)

Figure 12: Comparison of synthetic and calculated resonant modes after the last iteration

To demonstrate that our optimization procedure works also for more general orientations we have selected Test23. Again, we started the calculations using non-perturbed orientations (Table 1) as input parameter and optimized elasticity, geometry and shape using cubic constraints. To confirm the optimization was successful, we compare the perturbed orientations and dimensions with the ones refined during our cubic inversion. Table 5 shows the values of the refined and as-generated (perturbed) orientations and dimensions. The notation of crystallographic planes is shown in Figure 6. Crystallographic orientation of generated planes is given by normals to its faces (h,k,l). Number of completed iterations and number of successfully matched resonant modes utilized during each iteration was kept unchanged.

Table 5: Perturbed and refined orientations and dimensions

Face	Perturbed planes (h,k,l)	Refined planes (h,k,l)	Perturbed dimensions [mm]	Refined dimensions [mm]
red	(0.90, 0.33, 0.27)	(0.90, 0.34, 0.27)	3	3
blue	(-0.32, 0.95, -0.04)	(-0.32, 0.95, -0.04)	2.495	2.495
green	(0.71, 0.19, -0.68)	(0.71, 0.20, -0.68)	2.001	2.001

By comparing the results of the perturbed and refined orientations and dimensions, we can see that we have managed to successfully refine the orientations and dimensions again. This time however, we can see a small difference (0.5°) between refined and perturbed orientations for the scanned face (green). This difference is probably result of a wrong association of some resonant mode during the inversion procedure. The misfit between perturbed orientations and the ones used as an input in inverse calculations (Table 1) is 2.1° for the scanned face (green), 2.8° for the red and 2.3° for the blue face. The elastic coefficients for Test23 were determined as:

$$c_{11} = (169.84 \pm 1.30)\,\mathrm{GPa}$$

$$c_{12} = (120.10 \pm 0.99)\,\mathrm{GPa}$$

$$c_{44} = (59.79 \pm 1.02)\,\mathrm{GPa}$$

Figures 13 - 15 show practically same situation as for the Test3. With increasing number of performed iterations and successfully matched resonant modes the parameter Δf, characterizing the difference between synthetic resonant mode frequency and its calculated counterpart, is decreasing drastically. This time the parameter Δf was far greater in as generated data than for the Test3, but we have still managed to successfully optimize the data already after the first two iterations. The third and last iterations were performed to minimize the parameter Δf as much as possible. More iterations were not necessary, since desired precision was successfully achieved.

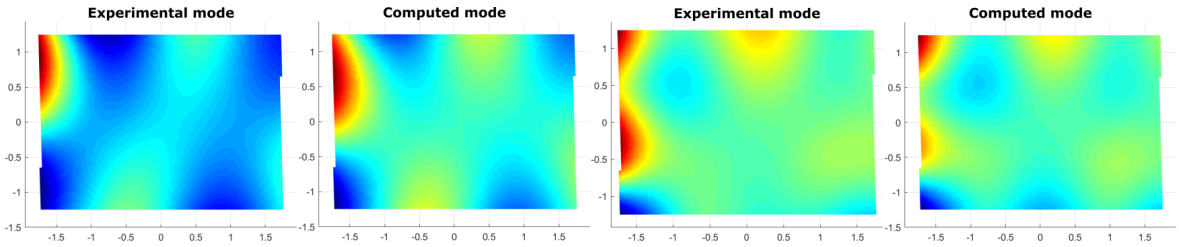

(a) Mode no. 20 ($\Delta f = 25{,}29$ kHz) (b) Mode no. 40 ($\Delta f = 16{,}28$ kHz)

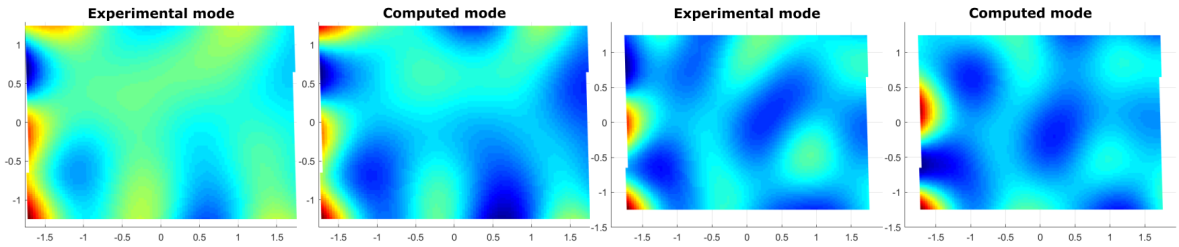

(c) Mode no. 63 ($\Delta f = 21{,}36$ kHz) (d) Mode no. 82 ($\Delta f = 21{,}89$ kHz)

Figure 13: Comparison of synthetic and calculated resonant modes at the start of the inversion

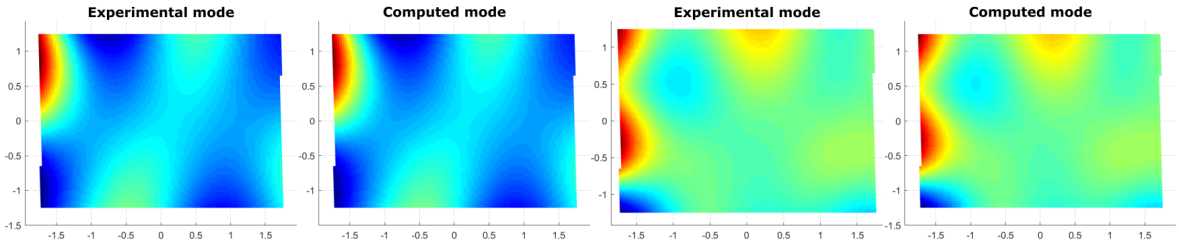

(a) Mode no. 20 ($\Delta f = 2{,}04$ kHz) (b) Mode no. 40 ($\Delta f = 2{,}62$ kHz)

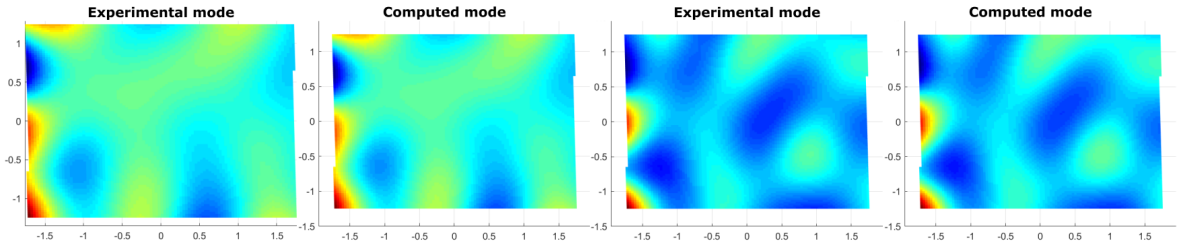

(c) Mode no. 63 ($\Delta f = 2{,}19$ kHz) (d) Mode no. 82 ($\Delta f = 3{,}48$ kHz)

Figure 14: Comparison of synthetic and calculated resonant modes after the second iteration

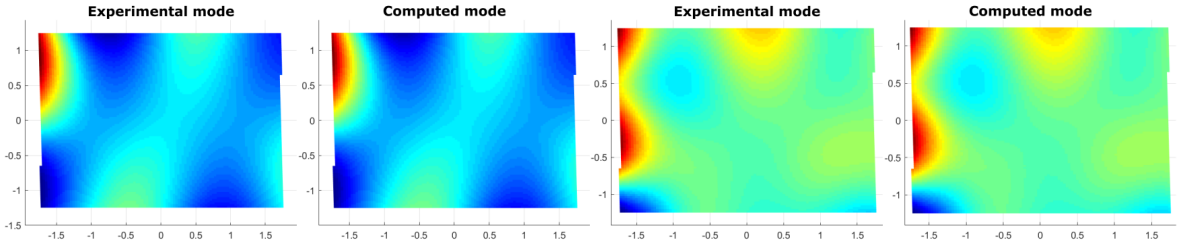

(a) Mode no. 20 ($\Delta f = 0{,}11$ kHz) (b) Mode no. 40 ($\Delta f = 0{,}04$ kHz)

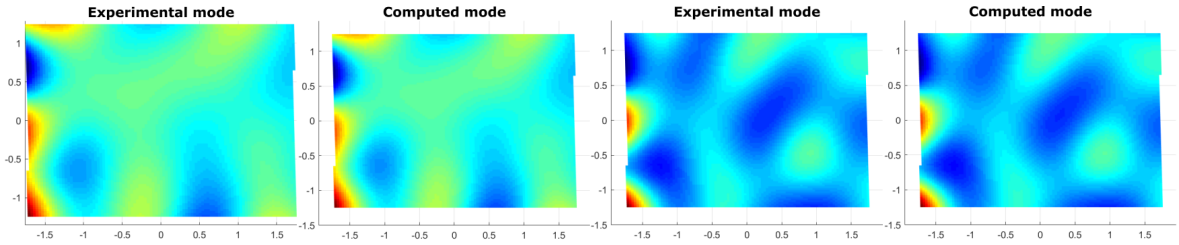

(c) Mode no. 63 ($\Delta f = 0{,}63$ kHz) (d) Mode no. 82 ($\Delta f = 0{,}69$ kHz)

Figure 15: Comparison of synthetic and calculated resonant modes after the last iteration

Figure 16 shows the evolution of parameter Δf for all selected resonant modes with increasing number of successful iteration. For all performed tests, parameter Δf is reduced drastically with each successful iteration.

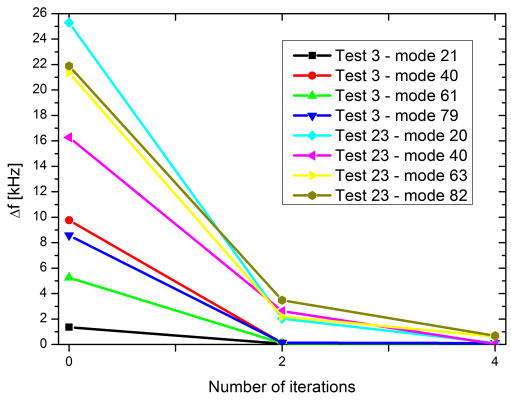

Figure 16: Evolution of the parameter Δf with increasing number of performed iterations

This two chosen examples fully represent the performance of the optimization procedure for all synthetic datasets. In all cases, a perfect match between the dimensions and orientations used for the generation of the synthetic spectra and those determined inversely was achieved. This indicates that the inverse procedure is well-posed and robust.

5.2 Experimental tests on single crystals

We tested the inverse procedure on the experimental RUS data for three samples, first being approximately in the principal orientation and the second and the third one being generally oriented.

The measurements ranged from 400 kHz to 3,5 MHz for the sample FeSi1 and from 200 kHz to 4 MHz for samples FeSi2 and FeSi3. During our calculations a Legendre polynomials of 25th degree (FeSi1) and 30th degree (FeSi2, FeSi3) were utilized to achieve a satisfactory precision alongside with fast computational speed.

The initial guesses for elastic constants used during the inversion calculations [29]:

$$c_{11} = 220\text{GPa}$$

$$c_{12} = 130\text{GPa}$$

$$c_{44} = 120\text{GPa}$$

All of the measurements were performed at room temperature (22°C) in an inert atmosphere of 20 mbar of nitrogen.

5.2.1 Sample cut along low-index planes (FeSi1)

The assumed orientations are shown in Table 6 (notation in Figure 6). Our aim for this sample is therefore to confirm and refine such measured orientation with high precision.

Table 6: Assumed crystallographic orientation of the sample FeSi1

Sample	Face	Planes (h, k, l)
FeSi1	red	(0, 0, -1)
	blue	(1, -1, 0)
	green	(1, 1, 0)

Values of longitudinal velocities obtained from pulse-echo measurements (described in paragraphs 2.2 and 3.1.), which are later used as a input parameter in RUS calculations for sample FeSi1, are shown in Table 7. These velocities are measured in the directions along the normal vector of each individual face (notation of the faces of the sample in Figure 6). It is important to precisely measure these velocities, as they are one of the highest contributors to the overall error of our calculations.

Table 7: Longitudinal velocities for three main directions for the sample FeSi1

Face	v_l [m/ms]
red	5.41
blue	6.26
green	6,27

By measuring the dimensions of the sample FeSi1 (shown in Table 8) and the mass of the sample ($m = 0,174$ g), we were able to calculate the density of the material, which as described in paragraph 2.1.4. is constant used in RUS calculations.

$$\rho = 7.63 \text{ g.cm}^{-3}$$

Table 8: Measured dimensions for sample FeSi1

Face	Dimensions [mm]
red	3.446
blue	3.277
green	2.007

For the sample FeSi1 we captured the resonant spectrum containing around 350 resonant peaks and their corresponding modal shapes. The biggest face of the sample was scanned in regular mesh of 32 x 32 points by scanning laser vibrometer with averaging from 50 pulses. Full measured spectrum can be seen on Figure 17.

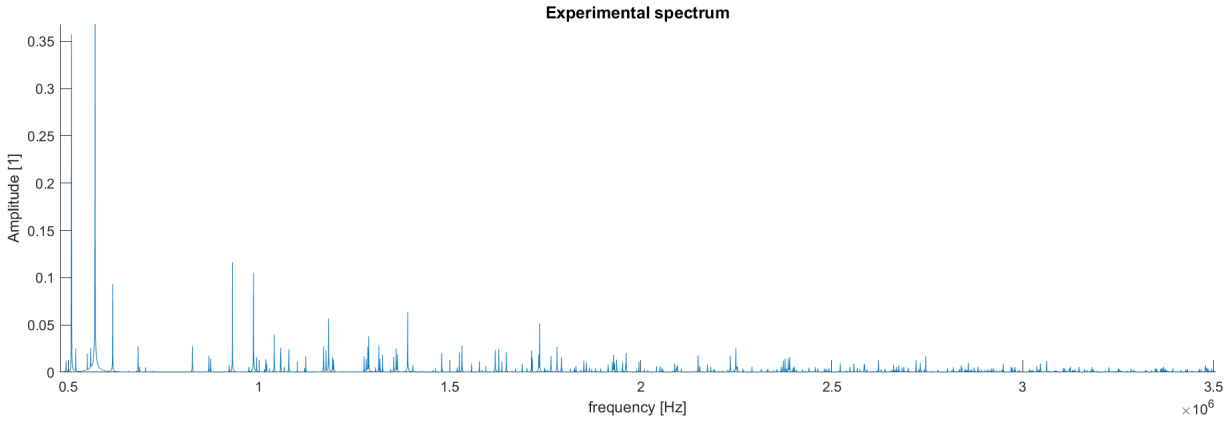

Figure 17: Measured spectrum for sample FeSi1

After several iterations, 180 out of 350 measured resonant peaks were matched successfully with their corresponding computed counterpart. Selected examples of matched modal shapes are shown in Figure 18.

Obtained elastic coefficients for sample FeSi1, using cubic symmetry:

$$c_{11} = (222.11 \pm 0.80)\,\text{GPa}$$

$$c_{12} = (135.14 \pm 0.84)\,\text{GPa}$$

$$c_{44} = (122.96 \pm 0.19)\,\text{GPa}$$

And the corresponding anisotropy ratio for this sample:

$$A = 2.83$$

After the satisfactory precision in elastic coefficients was achieved, we took a look at the refined crystallographic orientation and the dimensions of the sample FeSi1. Refined crystallographic orientation and dimensions can be seen in Table 9. The refined orientations and dimensions are very close to the expected values.

Table 9: Refined crystallographic orientations and dimensions of the sample FeSi1

Face	Planes (h, k, l)	Dimensions [mm]
red	(-0.02, -0.01, -0.99)	3.446
blue	(0.70, -0,72, -0.02)	3.289
green	(0.72, 0.69, -0.01)	1.998

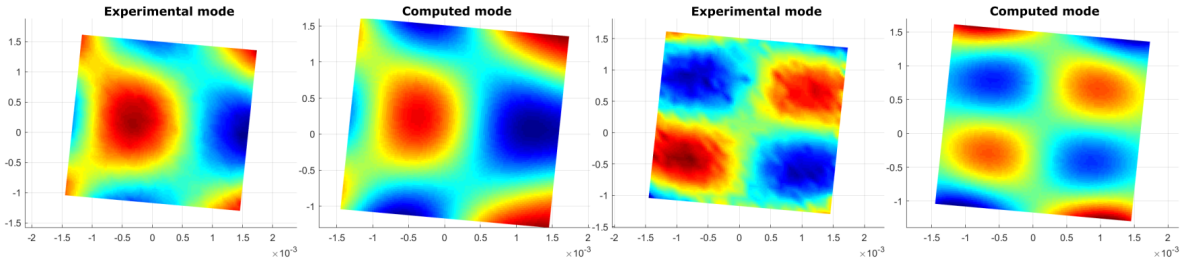

(a) Mode no. 16 ($\Delta f = 2{,}37$ kHz) (b) Mode no. 30 ($\Delta f = 1{,}92$ kHz)

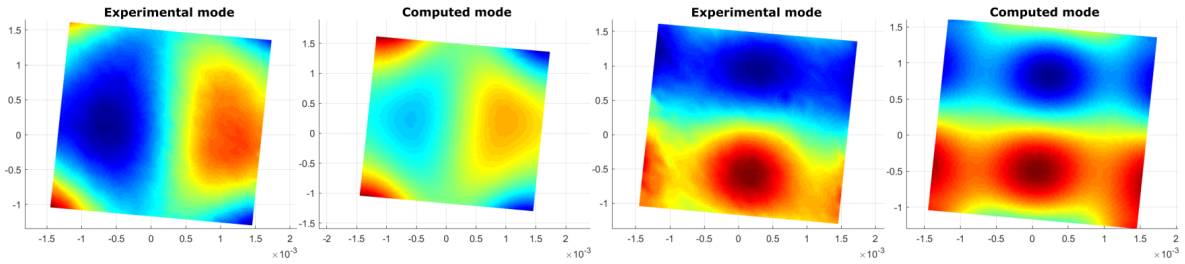

(c) Mode no. 45 ($\Delta f = 0{,}08$ kHz) (d) Mode no. 60 ($\Delta f = 5{,}81$ kHz)

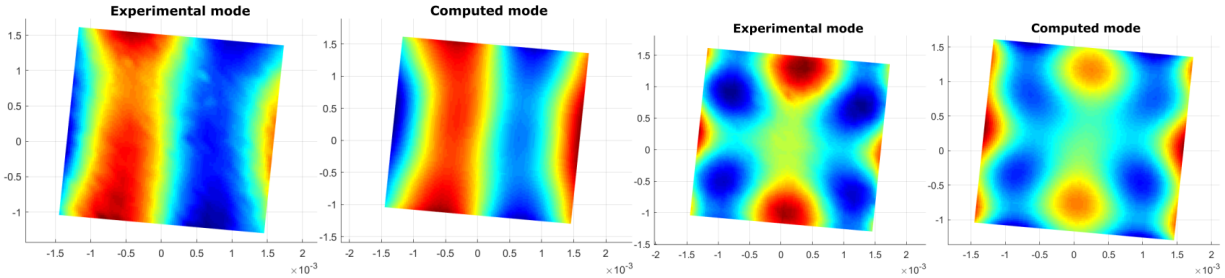

(e) Mode no. 72 ($\Delta f = 4{,}04$ kHz) (f) Mode no. 89 ($\Delta f = 0{,}58$ kHz)

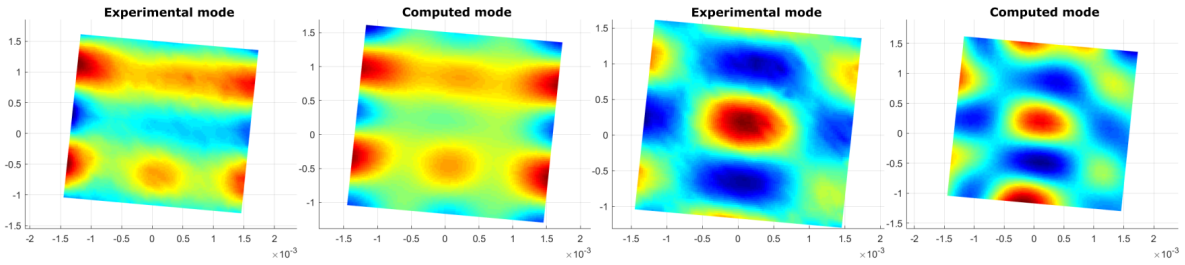

(g) Mode no. 103 ($\Delta f = 4{,}67$ kHz) (h) Mode no. 119 ($\Delta f = 3{,}07$ kHz)

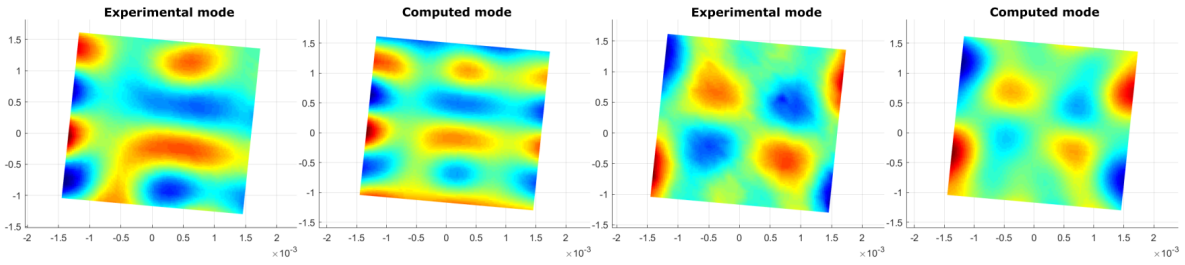

(i) Mode no. 132 ($\Delta f = 5{,}39$ kHz) (j) Mode no. 147 ($\Delta f = 5{,}13$ kHz)

Figure 18: Selected matched modal shapes of the sample FeSi1 after generalized inversion

5.2.2 Sample with one face along a low-index plane (FeSi2)

After the first sample FeSi1 was successfully measured and its parameters were established, we prepared the second sample FeSi2 with unknown crystallographic orientation of two of its faces (as described in paragraph 4.2.).

Again, we started with the pulse-echo measurements to complement the following RUS measurement. Values of longitudinal velocities obtained from pulse-echo measurements are shown in Table 10. These velocities are measured in the directions along the normal vector of each individual face (notation of the faces of the sample in Figure 6).

Table 10: Longitudinal velocities for three main directions for the sample FeSi2

Face	v_l [m/ms]
red	5.83
blue	6.42
green	6,28

Measured dimensions of the sample FeSi2 can be seen in Table 11. Mass of the sample FeSi2 was $m = 0,146$g and the corresponding calculated density of the material used in calculations:

$$\rho = 7.57 \text{ g.cm}^{-3}$$

Table 11: Measured dimensions for sample FeSi2

Face	Dimensions [mm]
red	3.140
blue	3.453
green	1.820

As for the sample FeSi2, we have managed to capture the resonant spectrum containing around 400 resonant peaks with their corresponding modal shapes. The biggest face of the sample was scanned in regular mesh of 40 x 40 points by scanning laser vibrometer with averaging from 50 pulses. Full measured spectrum can be seen on Figure 19.

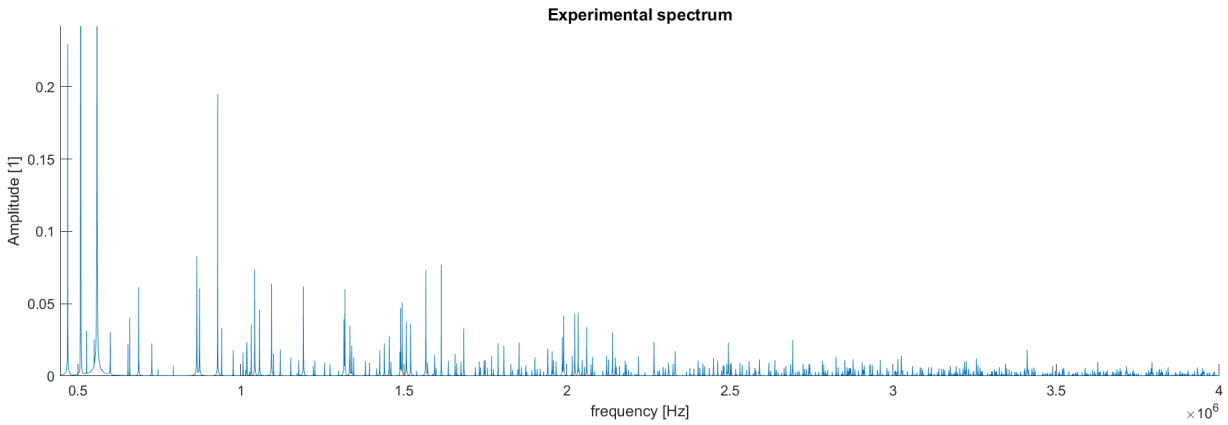

Figure 19: Measured spectrum for sample FeSi2

Refined orientations obtained for the sample FeSi1 were used as input parameters during the inverse procedure. After several iterations, 200 out of 400 measured resonant peaks were matched successfully with their corresponding computed counterpart. Selected examples of matched modal shapes are shown in Figure 20.

Obtained elastic coefficients for sample FeSi2, using cubic symmetry:

$$c_{11} = (220.48 \pm 0.70)\,\text{GPa}$$

$$c_{12} = (133.43 \pm 0.69)\,\text{GPa}$$

$$c_{44} = (122.26 \pm 0.15)\,\text{GPa}$$

And the corresponding anisotropy ratio for this sample:

$$A = 2.81$$

Alongside with the elastic coefficients calculations we were also able to determine the crystallographic orientations of the unknown faces and refine the measured dimensions of the sample FeSi2. Refined crystallographic orientations and dimensions can be seen in Table 12. Same as for the sample FeSi1, the refined orientations and dimensions are very close to the expected values.

Table 12: Refined crystallographic orientations and dimensions of the sample FeSi2

Face	Planes (h, k, l)	Dimensions [mm]
red	(-0.22, 0.21, -0.95)	3.141
blue	(0.67, -0.67, -0.31)	3.458
green	(0.70, 0.72, 0.01)	1.768

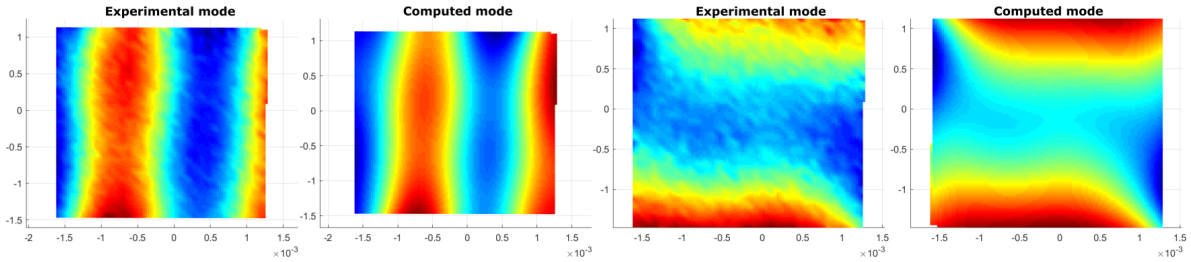

(a) Mode no. 15 ($\Delta f = 1{,}95$ kHz) (b) Mode no. 30 ($\Delta f = 0{,}08$ kHz)

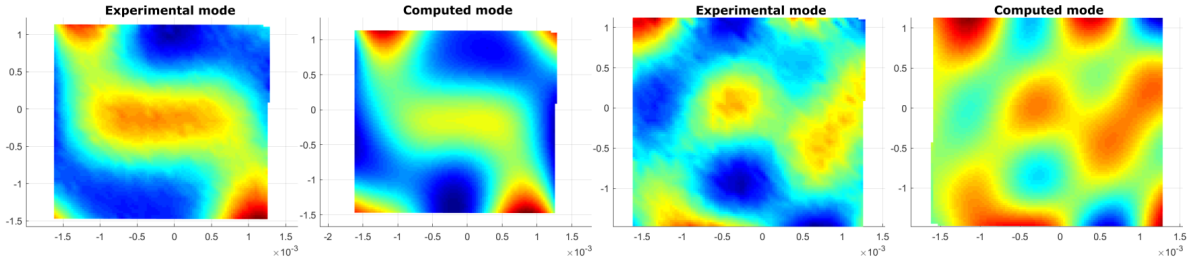

(c) Mode no. 43 ($\Delta f = 2{,}60$ kHz) (d) Mode no. 63 ($\Delta f = 3{,}01$ kHz)

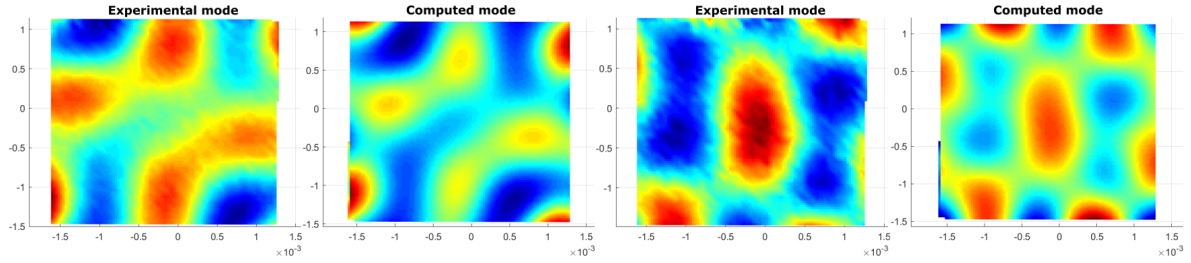

(e) Mode no. 75 ($\Delta f = 1{,}82$ kHz) (f) Mode no. 91 ($\Delta f = 3{,}14$ kHz)

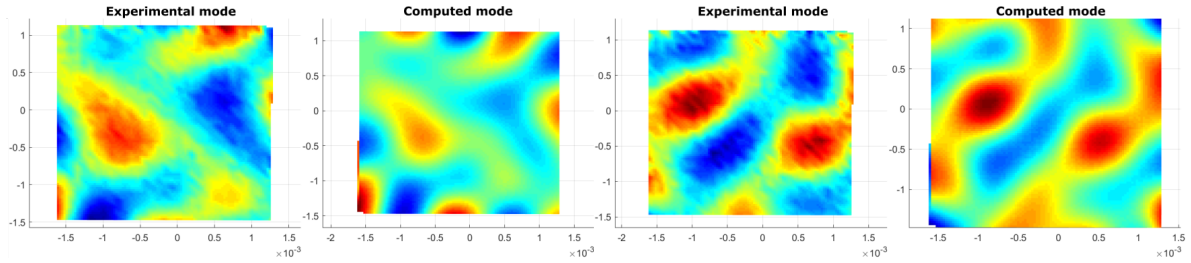

(g) Mode no. 104 ($\Delta f = 1{,}20$ kHz) (h) Mode no. 117 ($\Delta f = 1{,}04$ kHz)

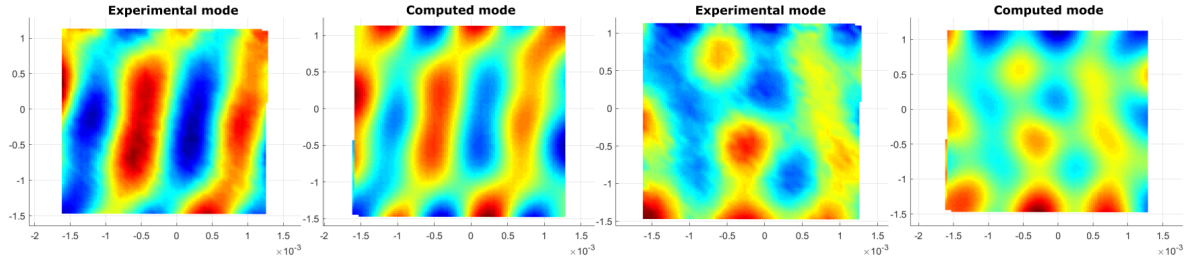

(i) Mode no. 126 ($\Delta f = 1{,}44$ kHz) (j) Mode no. 149 ($\Delta f = 2{,}97$ kHz)

Figure 20: Selected matched modal shapes of the sample FeSi2 after generalized inversion

5.2.3 A generally oriented sample (FeSi3)

Finally, to further complicate our calculations we prepared the third sample FeSi3 in a way that all three faces had unknown crystallographic orientation (as described in paragraph 4.2). Values of longitudinal velocities obtained from pulse-echo measurements are shown in Table 13. These velocities are measured in the directions along the normal vector of each individual face (notation of the faces of the sample in Figure 6).

Table 13: Longitudinal velocities for three main directions for the sample FeSi3

Face	v_l [m/ms]
red	5.83
blue	6.39
green	6.25

Measured dimensions of the sample FeSi3 can be seen in Table 14. Mass of the sample FeSi2 was $m = 0,061$g and the corresponding calculated density of the material used in calculations:

$$\rho = 7.50 \text{ g.cm}^{-3}$$

Table 14: Measured dimensions for sample FeSi3

Face	Dimensions [mm]
red	2.922
blue	3.136
green	0.895

Same as for the sample FeSi2, we have managed to capture the resonant spectrum containing around 400 resonant peaks with their corresponding modal shapes. The biggest face of the sample was scanned in regular mesh of 40 x 40 points, same as for the sample FeSi2, with averaging from 50 pulses. Full measured spectrum can be seen on Figure 21.

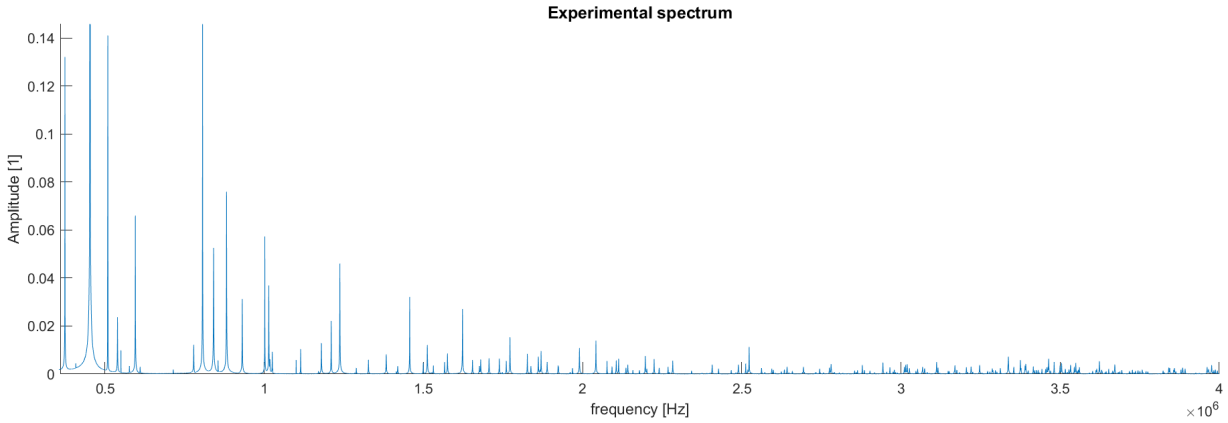

Figure 21: Measured spectrum for sample FeSi3

Refined orientations obtained for the sample FeSi2 were used as input parameters during the inverse procedure. After several iterations, 200 out of 400 measured resonant peaks were matched successfully with their corresponding computed counterpart. Selected examples of matched modal shapes are shown in Figure 22. Same as for the sample FeSi2 a Legendre polynomials of 30th degree were utilized in calculations.

Obtained elastic coefficients for sample FeSi3, using cubic symmetry:

$$c_{11} = (220.27 \pm 1.00)\,\text{GPa}$$

$$c_{12} = (132.78 \pm 0.98)\,\text{GPa}$$

$$c_{44} = (122.34 \pm 0.22)\,\text{GPa}$$

And the corresponding anisotropy ratio for this sample:

$$A = 2.80$$

Similar to sample FeSi2, besides the elastic coefficients optimization we were also able to determine the crystallographic orientations of all the faces and refine the measured dimensions of the sample FeSi3. Refined crystallographic orientations and dimensions can be seen in Table 15. The refined orientations and dimensions are very close to the expected values.

Table 15: Refined crystallographic orientations and dimensions of the sample FeSi3

Face	Planes (h, k, l)	Dimensions [mm]
red	(-0.20, 0.21, -0.96)	2.948
blue	(0.79, -0.55, -0.26)	3.133
green	(0.59, 0.81, 0.05)	0.881

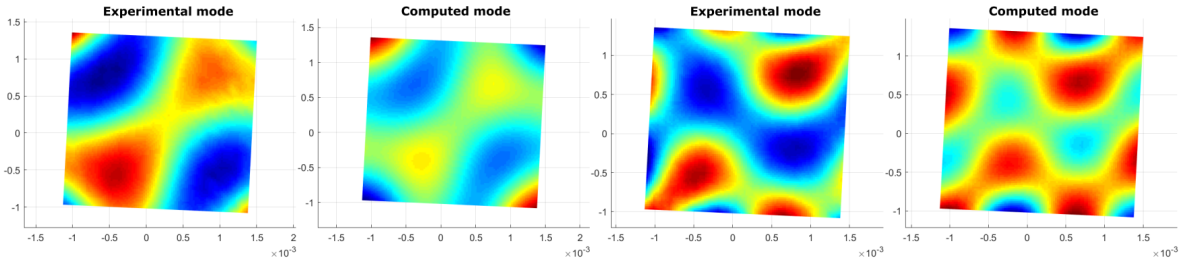

(a) Mode no. 16 ($\Delta f = 2{,}07$ kHz)

(b) Mode no. 31 ($\Delta f = 0{,}68$ kHz)

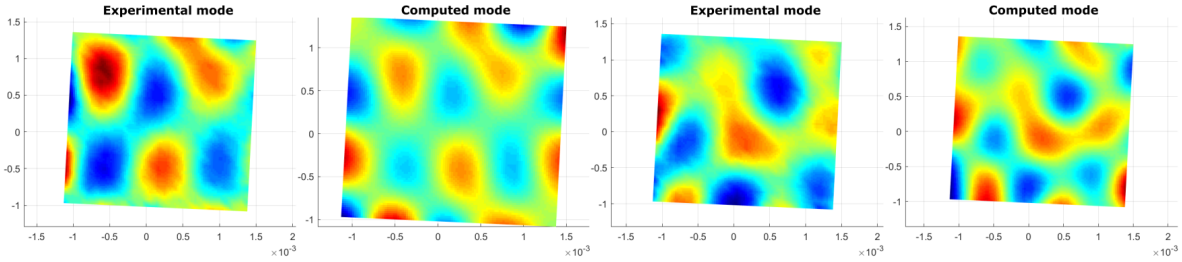

(c) Mode no. 46 ($\Delta f = 1{,}15$ kHz)

(d) Mode no. 58 ($\Delta f = 2{,}33$ kHz)

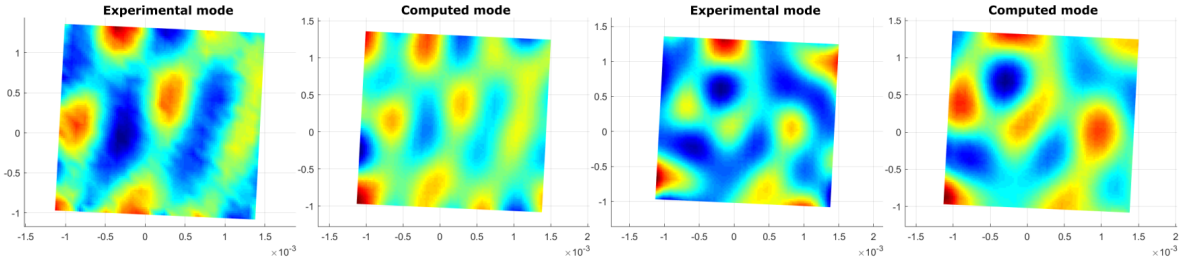

(e) Mode no. 74 ($\Delta f = 0{,}52$ kHz)

(f) Mode no. 87 ($\Delta f = 6{,}49$ kHz)

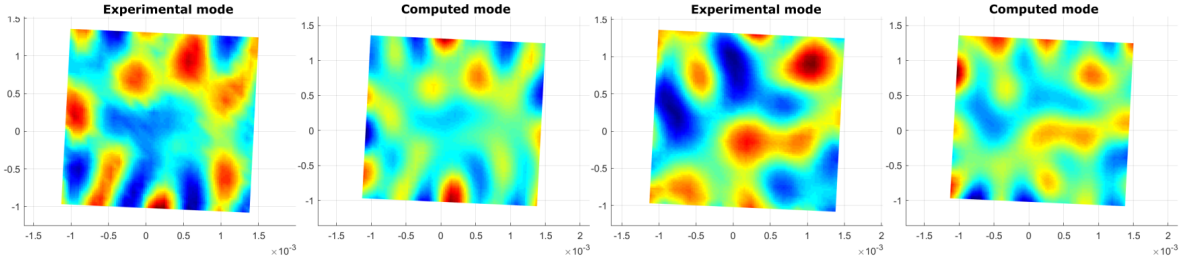

(g) Mode no. 137 ($\Delta f = 0{,}71$ kHz)

(h) Mode no. 150 ($\Delta f = 4{,}57$ kHz)

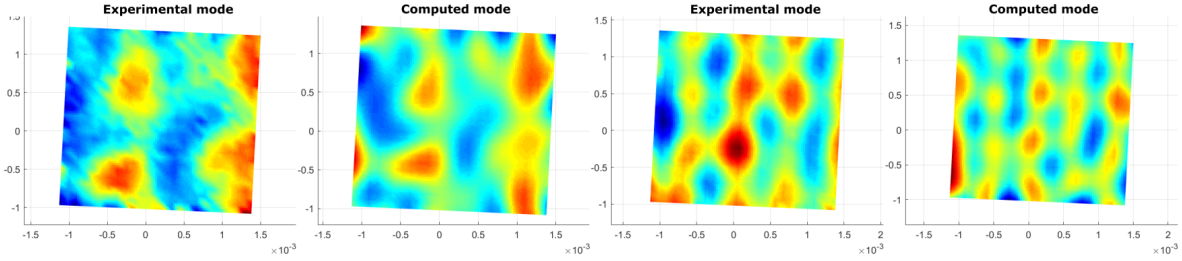

(i) Mode no. 165 ($\Delta f = 4{,}89$ kHz)

(j) Mode no. 179 ($\Delta f = 3{,}69$ kHz)

Figure 22: Selected matched modal shapes of the sample FeSi3 after generalized inversion

5.2.4 Discussion

Parameter Δf, shown for all selected modal shapes in each sample, characterizes the difference between measured resonant mode frequency and its calculated counterpart. In our case, higher values of this parameter are caused by the deviations in used crystallographic orientation compared to the real values but also by wrong association of some modal shapes which are used in our optimization procedure. With sample FeSi1, we have managed to obtain very high optimization with Δf not exceeding 0.5 % of each measured resonant frequency used in our calculations. Samples FeSi2 and FeSi3 were measured and optimized with even higher accuracy. For sample FeSi2 Δf did not exceed 0.2% of each measured resonant frequency used in optimization, while Δf for sample FeSi3 stayed within 0.3% of each measured resonant frequency utilized during inversion. So in summary, we were able to optimize all of the samples with desired precision.

All of the figures showing experimental modal shapes are noticeably smaller in means of the size of the scanned area than their computed counterparts. Usually, the signal obtained from a close proximity of the edges of the sample is weakened, sometimes not even registered at all, thus the scanning area was purposely moved further from the edges of the sample to obtain full rectangular image of the modal shapes without any missing points on the edges. This small change did not pose a significant problem during data evaluation. As can be seen, the sample FeSi1 was also scanned with smaller mesh and its parameters were calculated using lower order of the Legendre polynomials, since it was used as a control sample with established crystallographic orientation beforehand and thus did not need such precise measurement to refine its orientation, as was required for sample FeSi2 and FeSi3.

The differences in calculated elastic coefficients for each samples were mostly caused by using different densities of the material in each calculation. This problem could be easily avoided with by using one precisely measured value of the density of the material for all of the samples, and thus producing results for elastic coefficients with much lower deviation. Although the values of the parameter Δf for the sample FeSi1 are a little bit higher than for the other two samples, we have managed to optimize this sample with higher precision. The calculated errors are within 1% of their corresponding elastic constants for

each sample. All of the errors are thus in a reasonable range and suitable precision was achieved. However, the error could be reduced with higher number of successfully matched resonant modes used in optimization procedure, their precise revision after each iteration and by using higher order of the Legendre polynomials utilized in our calculations.

All of the errors were calculated using the equation (11). As mentioned above, one of the biggest contributors to the overall error was inaccurate measurement of the sound wave velocities during the pulse-echo measurements. However, it is very hard to eliminate such error, since as already mentioned, RUS does not allow accurate determination of c_{11} coefficient even when high number of modes is successfully matched and crystallographic orientation is accurately known and thus pulse-echo is used to complement RUS measurements. That is why the longitudinal velocity error was established as 0.02 m/ms.

The anisotropy ratios were calculated from established elastic coefficients using equation (21). The calculated values are close to value 3 and differ from each other by a very small margin, which means we have confirmed expected strong anisotropy of this material.

To confirm crystallographic orientations of all of the samples, established by our calculations, we have performed Laue diffraction experiment. Comparison between orientations from this experiment and the ones calculated by our generalized inversion can be seen in Table 16.

Table 16: Crystallographic orientations from Laue experiment

Sample	Face	Laue experiment (h, k, l)	Generalized inversion (h, k, l)
FeSi1	red	(-0.03, 0.02, -0.99)	(-0.02, -0.01, -0.99)
	blue	(-0.70, 0,71, 0.03)	(0.70, -0,72, -0.02)
	green	(-0.71, -0.70, 0.01)	(0.72, 0.69, -0.01)
FeSi2	red	(0.25, -0.26, -0.93)	(-0.22, 0.21, -0.95)
	blue	(-0.67, 0.66, -0.36)	(0.67, -0.67, -0.31)
	green	(-0.70, -0.71, 0.01)	(0.70, 0.72, 0.01)
FeSi3	red	(-0.25, 0.25, -0.93)	(-0.20, 0.21, -0.96)
	blue	(-0.77, 0.53, -0.35)	(0.79, -0.55, -0.26)
	green	(-0.59, -0.81, -0.06)	(0.59, 0.81, 0.05)

By comparing results of this experiment with the refined crystallographic orientations obtained by our generalized optimization procedure, we can see that the refined orientations deviate from the measured ones by a very small margin. Scanned face (green) exhibits smallest differences in orientation, while the other two faces differ from each other more. This difference rose from the fact that the Laue method is not able to establish orientations of the faces perpendicular to the measured one (red, blue) with very high precision. The difference between the orientations obtained from the Laue experiment and the ones calculated by our generalized inversion for the scanned face (green) are: 0.8° for the sample FeSi1, 0.4° for the sample FeSi2 and 0.6° for the sample FeSi3. We have thus managed to successfully reconstruct the orientation of the sample FeSi1 and precisely determined the unknown crystallographic orientations of the remaining two samples.

Finally, to show the importance of our extension of the optimization procedure, we tried calculating elastic coefficients of the sample FeSi1 using assumed crystallographic orientations (Table 6). When geometry and shape optimization is not utilized (we do not refine crystallographic orientations and use the ones measured by Laue experiment), but instead our classical approach to elastic coefficient calculations is used we can see the difference in measured resonant modal shapes and their computed counterparts (Figure 23). For comparison, same resonant modes but for the case of structure optimized by our generalized inversion procedure is shown in Figure 24. Not only is the parameter Δf reduced but it can be clearly seen that the modal shapes correspond to each other much better. This problem could lead to unsuccessful optimization and elastic constants calculation with unsuitable precision for the samples with bigger difference between real orientation and the one used during calculation. The extreme example is shown in Table 17, where we can see the difference between elastic coefficient calculated with refined orientations and dimensions (Table 12) using our generalized inversion and the ones calculated with assumed orientations (Table 6) using classical inversion procedure for more generally oriented sample FeSi2. The difference between real orientation and the one used as a input in inverse calculations was only 0,8° for the scanned face, but more than 21° for the remaining ones.

Table 17: Difference in the elastic coefficients calculated using generalized and classical inversion for the sample FeSi2

Elastic coefficient	Refined orientations, generalized inversion	Assumed orientations, classical inversion
c_{11} [GPa]	220.48±0.70	247.10±2.30
c_{12} [GPa]	133.43±0.69	152.49±2.01
c_{44} [GPa]	122.26±0.15	108.61±1.94

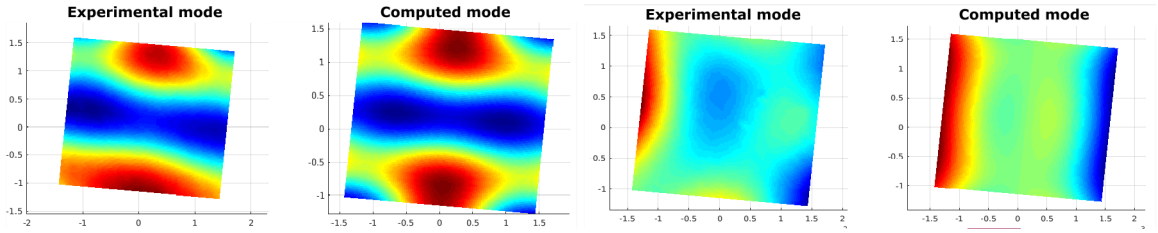

(a) Mode no. 23 (Δf = 7,38 kHz) (b) Mode no. 33 (Δf = 6,75 kHz)

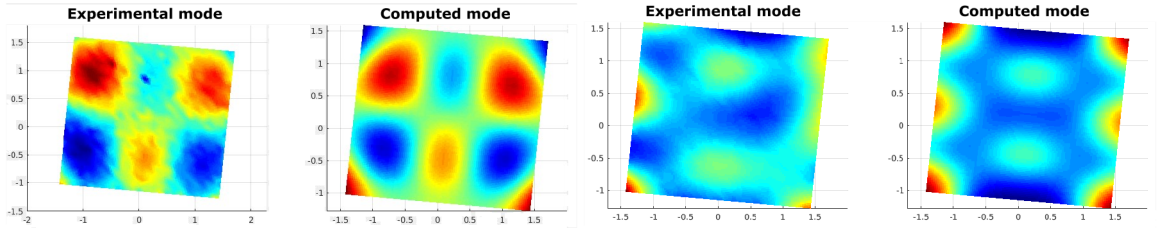

(c) Mode no. 44(Δf = 3,66 kHz) (d) Mode no. 77 (Δf = 5,87 kHz)

Figure 23: Selected resonant modes after using assumed geometry and classical inversion

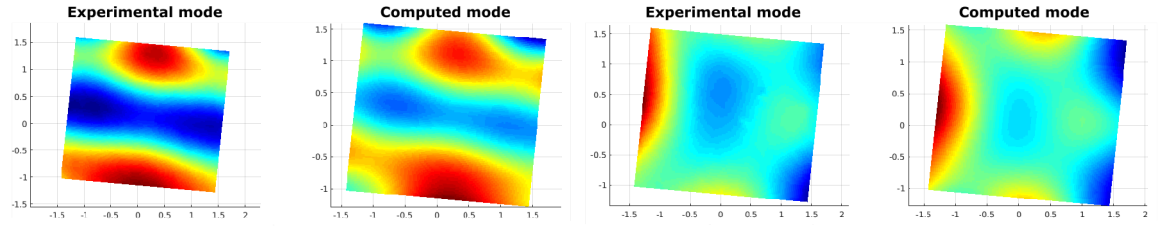

(a) Mode no. 23 (Δf = 2,62 kHz) (b) Mode no. 33 (Δf = 3,82 kHz)

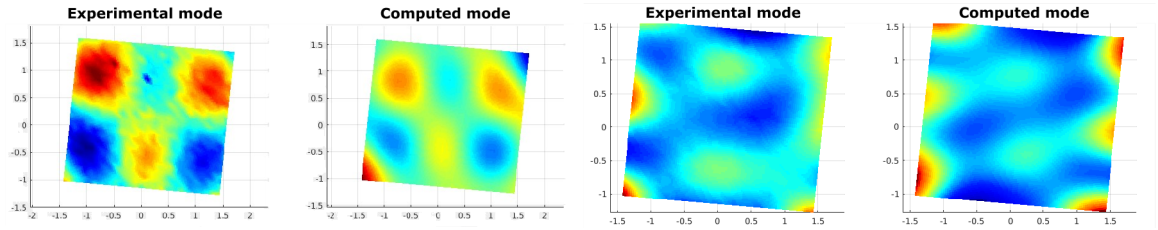

(c) Mode no. 44 (Δf = 2,50 kHz) (d) Mode no. 77 (Δf = 3,06 kHz)

Figure 24: Selected resonant modes after using refined geometry and generalized inversion

5.3 Observation of the cubicity in metastable beta-Ti alloys

Multi-phase β-Ti crystals exhibited much higher damping than FeSi single crystals, which means that obtained spectra and therefore the number of successfully matched resonant modes is much smaller. However, the measurements were sufficient enough to perform our cubic optimization successfully.

We proceeded in two steps:

1) shape and orientation optimization, assuming cubic symmetry,

which results in $\widetilde{T}_{ijkl}^{cubic}$(optimized cubic composite function)

2) triclinic symmetry inversion with fixed dimensions and orientations from 1),

which results in $\widetilde{T}_{ijkl}$

Such calculated "quasi-tensor" $\widetilde{T}_{ijkl}$ differs from the optimized cubic composite function by some $\delta\widetilde{T}$ ($\widetilde{T}_{ijkl} = \widetilde{T}_{ijkl}^{cubic} + \delta\widetilde{T}$). If this difference $\delta\widetilde{T}$ stays very small, we can say that the material retained its former cubic symmetry after the phase transformation. So by comparing the differences between cubic and triclinic inversions, we can obtain the information about possible changes in the symmetry of the material after the phase transformation.

We selected 2 types of metastable beta-titanium alloys: LCB and Ti-15Mo. From these materials, we have chosen 4 samples of LCB alloy and 5 samples of Ti-15Mo alloy which underwent different heat treatment. Basic information about the alloys, each sample and comparison of their corresponding heat treatment are shown in Table 3.

All of the measurements ranged from 300 kHz up to 2,5 MHz. Obtained spectra contained around 80 - 120 resonant peaks for each sample, from which more than 75% were successfully associated with their corresponding computed counterpart. Legendre polynomials of the 30th order were utilized during inversion calculations. Density $\rho =$ 4.77 g.cm^{-3}was used for the LCB alloy and $\rho = 4.93$ g.cm^{-3} for the Ti15Mo alloy.

We ran our optimization procedure to refine dimensions and crystallographic orientation of each sample and used such optimized association of the resonant modes as an input in fully triclinic inversion calculations.

We start with the LCB alloy. We ran our optimization procedure to refine dimensions and crystallographic orientation of each sample. Table 18 shows refined dimensions

and Table 19 shows refined crystallographic orientations of each sample after our cubic optimization. Crystallographic orientation of the sample is given by normals to its faces (h,k,l). Notation of the faces of the sample in Figure 6.

Table 18: Refined dimensions [mm]

Sample	red	blue	green
LCB_m8h1	3.773	2.410	1.942
LCB_mono8h2	3.774	2.411	1.931
LCB_mono128h2	3.3	3.011	2.023
LCB_ST2_tc750	3.255	2.149	1.499

Table 19: Refined orientation (h, k, l)

Sample	red	blue	green
LCB_m8h1	(0.89, 0.44, 0.09)	(-0.40, 0.82, -0.40)	(-0.19, 0.3, 0.93)
LCB_mono8h2	(0.89, 0.44, 0.09)	(-0.40, 0.82, -0.40)	(-0.19, 0.3, 0.93)
LCB_mono128h2	(0.91, 0.39, 0.13)	(-0.31, 0.86, -0.41)	(-0.27, 0.29, 0.92)
LCB_ST2_tc750	(0.90, -0.43, 0.09)	(0.38, 0.82, 0.43)	(-0.29, -0.38, 0.87)

Corresponding elastic coefficients for each sample using cubic symmetry are shown in Table 20.

Table 20: Obtained elastic coefficients [GPa]

Sample	c_{11}	c_{12}	c_{44}
LCB_m8h1	159.77±0.40	86.71±0.38	58.25±0.04
LCB_mono8h2	159.47±0.60	86.22±0.57	58.01±0.08
LCB_mono128h2	164.83±0.70	86.74±0.69	58.94±0.26
LCB_ST2_tc750	146.19±0.60	72.79±0.64	49.53±0.14

After the successful geometry and shape optimization using cubic symmetry was performed, we used such optimized association of the resonant modes for fully triclinic inversion calculations.

Calculated elastic coefficients for the sample LCB_m8h1 using triclinic symmetry:

$$c_{ij} = \begin{pmatrix} 159.36 \pm 1.16 & 86.99 \pm 0.86 & 86.34 \pm 0.97 & 1.24 \pm 0.68 & 0.22 \pm 0.91 & -0.04 \pm 0.47 \\ & 160.59 \pm 1.29 & 87.17 \pm 0.79 & 1.27 \pm 0.70 & 0.98 \pm 1.02 & 0.11 \pm 0.49 \\ & & 159.69 \pm 1.17 & 0.59 \pm 0.69 & -0.01 \pm 0.98 & -0.09 \pm 0.51 \\ & & & 57.81 \pm 0.24 & -0.18 \pm 0.17 & 0.43 \pm 0.28 \\ & & & & 58.015 \pm 0.29 & -0.33 \pm 0.25 \\ & & & & & 58.24 \pm 0.28 \end{pmatrix} \text{GPa}$$

Elastic coefficients for the sample LCB_mono8h2 using triclinic symmetry:

$$c_{ij} = \begin{pmatrix} 160.99 \pm 1.09 & 87.74 \pm 0.71 & 87.74 \pm 0.80 & 1.12 \pm 0.60 & 0.29 \pm 0.90 & -0.72 \pm 0.40 \\ & 158.05 \pm 1.14 & 86.15 \pm 0.85 & 0.41 \pm 0.63 & 0.79 \pm 1.03 & -0.63 \pm 0.49 \\ & & 159.22 \pm 0.92 & 0.55 \pm 0.56 & 0.36 \pm 0.96 & -1.08 \pm 0.56 \\ & & & 57.81 \pm 0.27 & 0.11 \pm 0.21 & -0.23 \pm 0.29 \\ & & & & 57.81 \pm 0.29 & 0.13 \pm 0.21 \\ & & & & & 58.29 \pm 0.23 \end{pmatrix} \text{GPa}$$

Elastic coefficients for the sample LCB_mono128h2 using triclinic symmetry:

$$c_{ij} = \begin{pmatrix} 167.51 \pm 1.79 & 82.87 \pm 1.03 & 87.86 \pm 1.80 & -0.02 \pm 0.78 & 1.45 \pm 1.08 & -0.98 \pm 0.91 \\ & 157.84 \pm 1.82 & 84.07 \pm 1.21 & -0.59 \pm 0.74 & 1.73 \pm 1.23 & -4.05 \pm 0.86 \\ & & 168.32 \pm 1.49 & 0.61 \pm 0.73 & 3.32 \pm 1.14 & -1.54 \pm 0.94 \\ & & & 57.83 \pm 0.45 & -0.63 \pm 0.27 & -0.63 \pm 0.29 \\ & & & & 59.68 \pm 0.41 & -0.36 \pm 0.39 \\ & & & & & 58.69 \pm 0.47 \end{pmatrix} \text{GPa}$$

Elastic coefficients for the sample LCB_ST2_tc750 using triclinic symmetry:

$$c_{ij} = \begin{pmatrix} 144.32 \pm 2.08 & 72.64 \pm 1.04 & 71.13 \pm 1.39 & 0.09 \pm 1.11 & -0.68 \pm 1.51 & 0.45 \pm 0.95 \\ & 148.60 \pm 2.19 & 73.53 \pm 1.31 & -0.49 \pm 1.09 & -0.76 \pm 1.61 & 0.70 \pm 0.93 \\ & & 144.92 \pm 1.83 & -0.32 \pm 1.10 & -1.09 \pm 1.49 & 0.42 \pm 0.94 \\ & & & 49.15 \pm 0.47 & 0.18 \pm 0.33 & 0.09 \pm 0.41 \\ & & & & 49.57 \pm 0.51 & 0.19 \pm 0.42 \\ & & & & & 49.33 \pm 0.48 \end{pmatrix} \text{GPa}$$

Figure 25 shows few of the highest successfully matched resonant modes for each sample along with the parameter Δf, which characterizes difference between measured resonant mode frequency and its calculated counterpart. We can see that for each selected resonant mode utilized in optimization process the parameter Δf does not exceed even 0.5 % of the measured resonant frequency utilized in inversion. That means that sufficient precision of optimization was achieved. All of the errors were calculated using the equation (11). The biggest contributor to the overall error was inaccurate measurement of the sound wave velocities during the pulse-echo measurements. Error of the velocity measurement was established as 0.02 m/ms. After the cubic inversion the error of elastic coefficients did not exceed 1 % of corresponding calculated constant for every sample. All of the errors are thus in a reasonable range and suitable precision was achieved.

However, even better precision could be achieved with higher number of successfully matched resonant modes, their precise revision after each iteration and by using higher order of the Legendre polynomials.

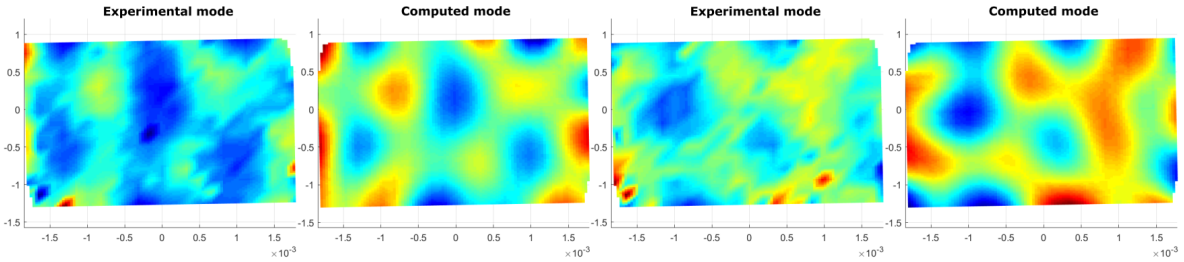

(a) LCB_m8h1 mode no. 75 (Δf = 0,47 kHz) (b) LCB_m8h1 mode no. 77 (Δf = 0,89 kHz)

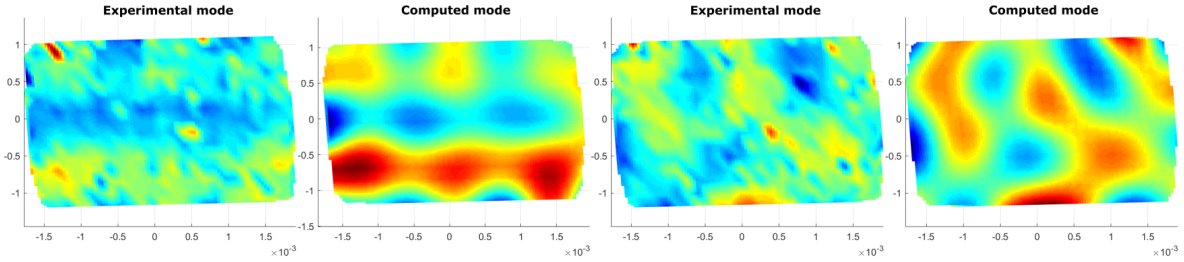

(c) LCB_mono8h2 mode no. 64 (Δf = 3.61 kHz) (d) LCB_mono8h2 mode no. 65 (Δf = 0,54 kHz)

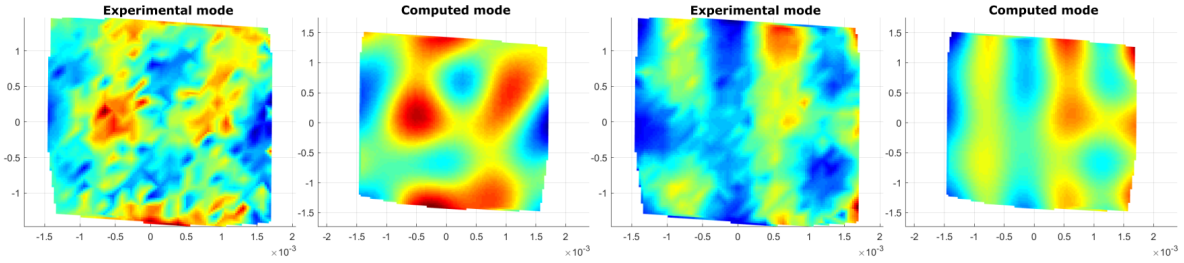

(e) LCB_mono128h2 mode no. 81 (Δf = 3.08 kHz)(f) LCB_mono128h2 mode no. 84 (Δf = 4,76 kHz)

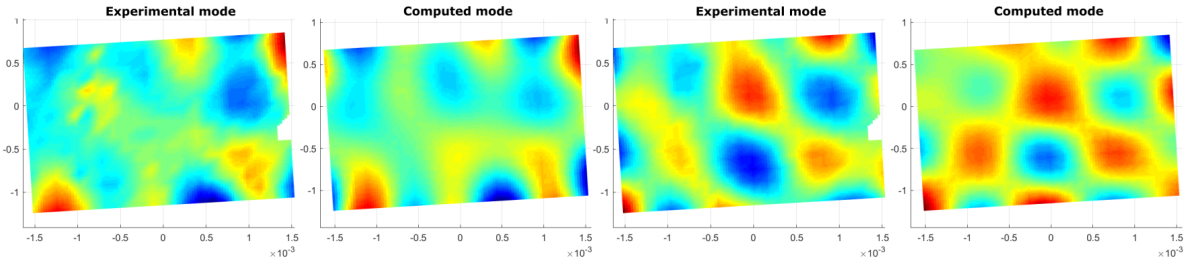

(g) LCB_ST2_tc750 mode no. 103 (Δf = 2,84 kHz) (h) LCB_ST2_tc750 mode no. 105 (Δf = 0,49 kHz)

Figure 25: Selected matched modal shapes of the LCB alloy samples after generalized inversion

To compare the difference between cubic optimization and full triclinic inversion, we have plotted cut of the Young's modulus in the direction of uniaxial load (plane (110)) in polar coordinates. Results are shown in Figure 26. Blue line represents Young's modulus calculated from cubic optimization results, while dashed orange line represents Young's modulus calculated from results of the triclinic inversion. We can see that all of the samples have managed to retain their former cubic symmetry after the phase transition within experimental error. Heat treatment did not cause any change of the symmetry of the material after the phase transformation.

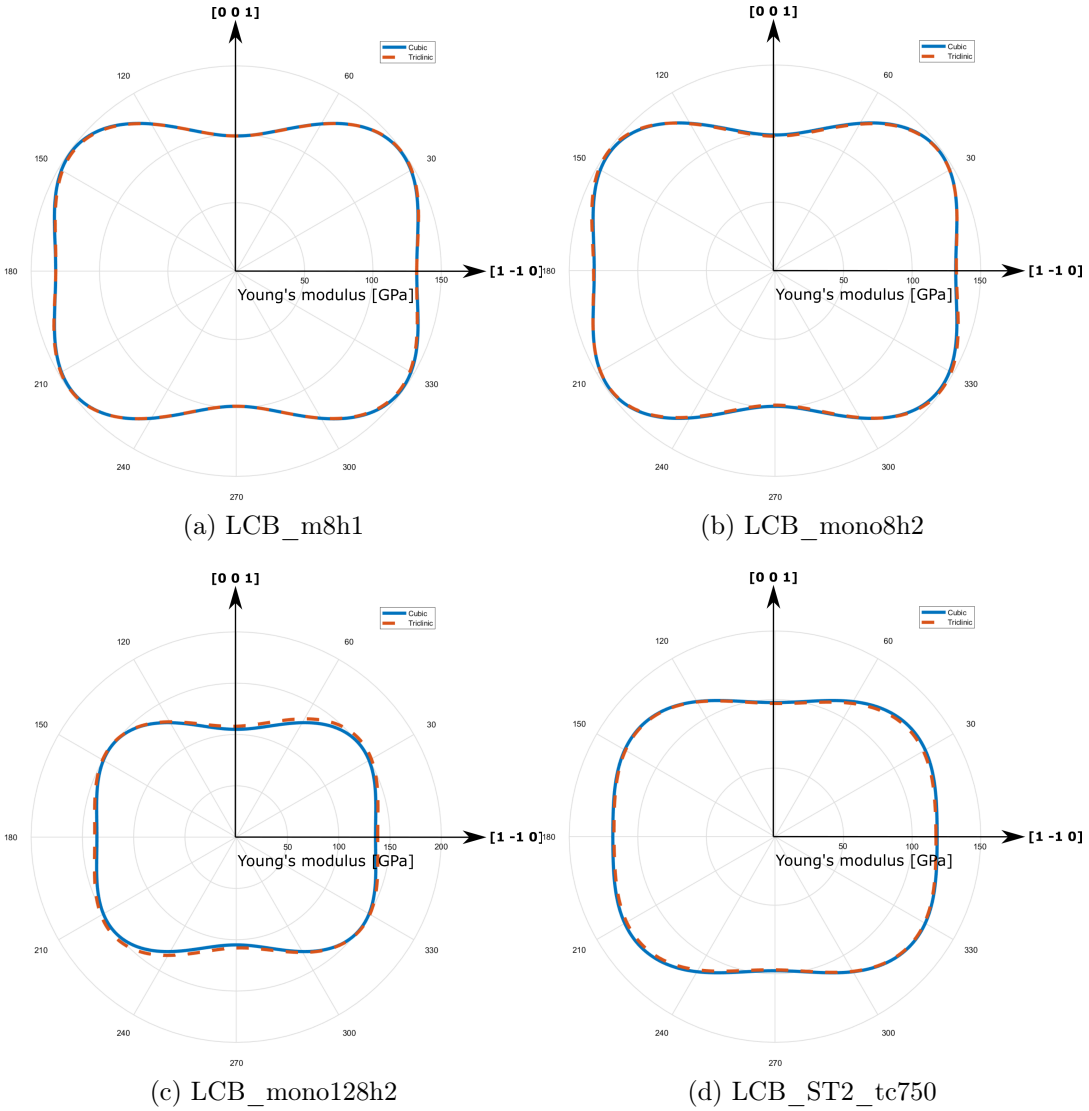

(a) LCB_m8h1 (b) LCB_mono8h2

(c) LCB_mono128h2 (d) LCB_ST2_tc750

Figure 26: (110)-cuts of Young's modulus surfaces for the optimal cubic (solid line) and triclinic (dashed line) fits

After the successful analysis of the LCB alloy we switch our focus to the Ti-15Mo. Table 21 shows refined dimensions and Table 22 shows refined crystallographic orientations of each sample after our cubic optimization. Crystallographic orientation of the sample is given by normals to its faces (h,k,l). Notation of the faces of the sample in Figure 6.

Table 21: Refined dimensions [mm]

Sample	red	blue	green
Ti15Mo_AB_tc750	2.689	2.671	1.859
Ti15Mo_L	4.528	2.548	2.813
Ti15Mo_R_po400	4.345	2.603	2.179
Ti15Mo_V	4.822	3.071	1.717
Ti15Mo_W	4.856	3.030	1.617

Table 22: Refined orientation (h, k, l)

Sample	red	blue	green
Ti15Mo_AB_tc750	(-0.81, 0.43, -0.40)	(0.05, -0.64, -0.77)	(-0.59, -0.63, 0.51)
Ti15Mo_L	(0.59, -0.60, 0.54)	(-0.37, 0.38, -0.85)	(-0.72, -0.69, 0.01)
Ti15Mo_R_po400	(0.52, -0.65, 0.55)	(-0.37, 0.41, 0.83)	(-0.76, -0.65, -0.03)
Ti15Mo_V	(0.30, -0.53, -0.79)	(-0.77, -0.63, -0.10)	(-0.61, -0.58, -0.53)
Ti15Mo_W	(-0.07, 0.72, -0.69)	(0.79, -0.39, -0.47)	(-0.61, -0.58, -0.53)

Corresponding elastic coefficients for each sample using cubic symmetry are shown in Table 23.

Table 23: Obtained elastic coefficients [GPa]

Sample	c_{11}	c_{12}	c_{44}
Ti15Mo_AB_tc750	149.66±0.70	92.55±0.66	47.36±0.11
Ti15Mo_L	154.41±0.60	87.82±0.62	53.90±0.12
Ti15Mo_R_po400	168.26±0.50	85.59±0.51	58.39±0.07
Ti15Mo_V	159.12±0.60	87.31±0.55	55.01±0.08
Ti15Mo_W	159.95±0.6	89.51±0.57	54.49±0.06

After the successful geometry and shape optimization using cubic symmetry was performed, we used such optimized association of the resonant modes for fully triclinic inversion calculations.

Elastic coefficients for the sample Ti15Mo_AB_tc750 using triclinic symmetry:

$$c_{ij} = \begin{pmatrix} 151.22 \pm 1.77 & 94.46 \pm 1.39 & 91.27 \pm 1.38 & 0.36 \pm 0.66 & 1.62 \pm 1.33 & 0.84 \pm 1.18 \\ & 151.17 \pm 2.47 & 92.13 \pm 1.02 & -0.26 \pm 0.63 & 1.10 \pm 1.35 & -0.05 \pm 1.19 \\ & & 146.92 \pm 2.41 & 0.29 \pm 0.64 & 1.02 \pm 1.19 & 0.07 \pm 1.17 \\ & & & 46.95 \pm 0.33 & -0.54 \pm 0.39 & -0.51 \pm 0.33 \\ & & & & 47.08 \pm 0.51 & 0.02 \pm 0.20 \\ & & & & & 48.03 \pm 0.46 \end{pmatrix} \text{GPa}$$

Elastic coefficients for the sample Ti15Mo_L using triclinic symmetry:

$$c_{ij} = \begin{pmatrix} 152.89 \pm 5.07 & 87.95 \pm 1.17 & 87.91 \pm 2.54 & -1.52 \pm 2.43 & -1.36 \pm 2.58 & 1.41 \pm 1.04 \\ & 156.66 \pm 4.71 & 89.43 \pm 2.59 & -2.11 \pm 2.49 & -0.34 \pm 2.61 & -0.39 \pm 1.02 \\ & & 155.35 \pm 1.94 & -0.01 \pm 2.40 & 1.21 \pm 2.48 & 0.18 \pm 0.64 \\ & & & 54.15 \pm 0.85 & -0.30 \pm 0.26 & -0.91 \pm 0.54 \\ & & & & 53.17 \pm 0.81 & -0.02 \pm 0.56 \\ & & & & & 53.79 \pm 0.34 \end{pmatrix} \text{GPa}$$

Elastic coefficients for the sample Ti15Mo_R_po400 using triclinic symmetry:

$$c_{ij} = \begin{pmatrix} 159.02 \pm 2.50 & 83.52 \pm 0.92 & 82.15 \pm 1.72 & -1.76 \pm 1.19 & -4.01 \pm 1.25 & 2.32 \pm 0.67 \\ & 174.14 \pm 2.55 & 90.61 \pm 1.49 & -4.19 \pm 1.16 & -2.79 \pm 1.36 & 1.64 \pm 0.67 \\ & & 170.78 \pm 1.54 & -4.38 \pm 1.21 & -4.38 \pm 1.32 & 1.41 \pm 0.61 \\ & & & 58.94 \pm 0.52 & 0.13 \pm 0.23 & 0.16 \pm 0.33 \\ & & & & 58.94 \pm 0.53 & 0.54 \pm 0.36 \\ & & & & & 58.14 \pm 0.28 \end{pmatrix} \text{GPa}$$

Elastic coefficients for the sample Ti15Mo_V using triclinic symmetry:

$$c_{ij} = \begin{pmatrix} 154.59 \pm 4.59 & 86.43 \pm 1.55 & 84.55 \pm 2.94 & -0.96 \pm 1.19 & -2.97 \pm 1.73 & 0.65 \pm 1.28 \\ & 162.73 \pm 5.34 & 89.58 \pm 2.36 & -0.54 \pm 1.19 & -2.88 \pm 1.74 & -0.79 \pm 0.98 \\ & & 158.05 \pm 2.98 & -2.43 \pm 1.57 & -3.90 \pm 1.83 & 0.01 \pm 0.95 \\ & & & 55.59 \pm 0.98 & 0.05 \pm 0.49 & -0.43 \pm 0.45 \\ & & & & 54.61 \pm 0.84 & -1.41 \pm 0.54 \\ & & & & & 54.26 \pm 0.52 \end{pmatrix} \text{GPa}$$

Elastic coefficients for the sample Ti15Mo_W using triclinic symmetry:

$$c_{ij} = \begin{pmatrix} 156.67 \pm 3.95 & 90.48 \pm 5.07 & 85.52 \pm 4.58 & -0.12 \pm 1.09 & 0.59 \pm 3.23 & -2.47 \pm 3.18 \\ & 160.25 \pm 8.76 & 88.33 \pm 2.28 & 0.54 \pm 1.41 & 0.31 \pm 3.42 & 2.56 \pm 3.21 \\ & & 159.43 \pm 9.82 & 0.13 \pm 1.72 & -5.03 \pm 2.96 & -1.46 \pm 3.34 \\ & & & 54.86 \pm 0.66 & -1.85 \pm 0.95 & 1.57 \pm 0.88 \\ & & & & 52.73 \pm 1.12 & 1.21 \pm 0.54 \\ & & & & & 53.75 \pm 1.15 \end{pmatrix} \text{GPa}$$

Figure 27 shows few of the highest successfully matched resonant modes for each sample along with the parameter Δf. Same as for the LCB alloy, the parameter Δf does not exceed 0.5 % of the measured resonant frequency utilized in inversion and error of elastic coefficients does not exceed 1 % of corresponding calculated constant for every sample, which means that sufficient precision of optimization was achieved.

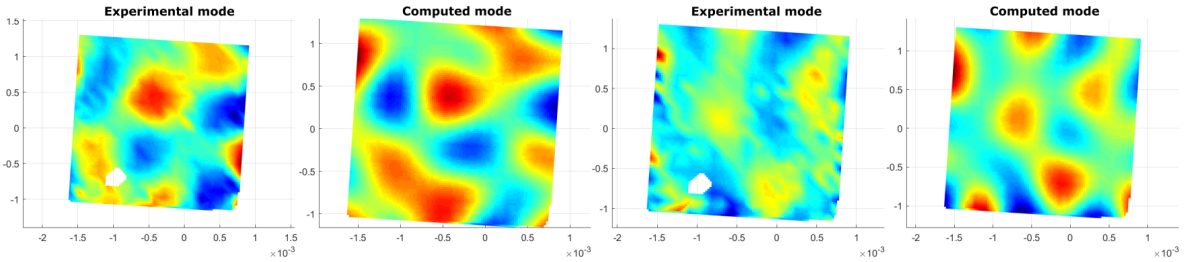

(a) Ti15Mo_AB_tc750 mode no. 122 ($\Delta f = 3{,}54$ kHz)

(b) Ti15Mo_AB_tc750 mode no. 123 ($\Delta f = 2{,}74$ kHz)

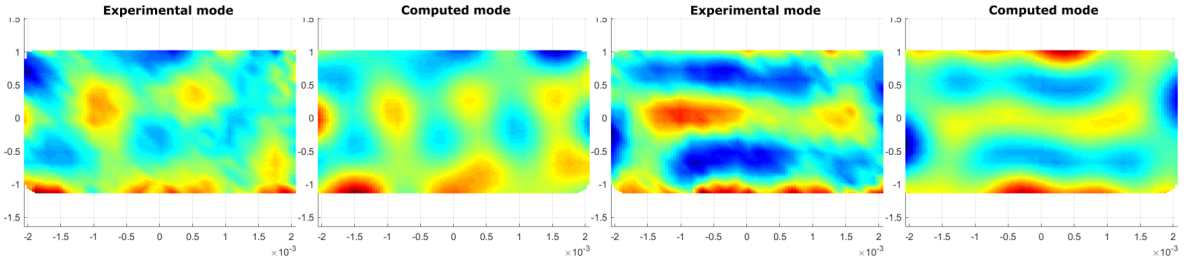

(c) Ti15Mo_L mode no. 142 ($\Delta f = 0{,}49$ kHz)

(d) Ti15Mo_L mode no. 147 ($\Delta f = 2{,}34$ kHz)

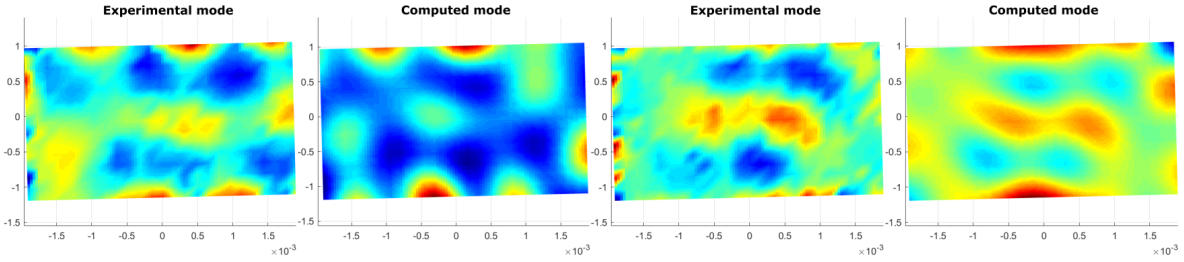

(e) Ti15Mo_R_po400 mode no. 121 ($\Delta f = 0{,}36$ kHz)

(f) Ti15Mo_R_po400 mode no. 131 ($\Delta f = 0{,}35$ kHz)

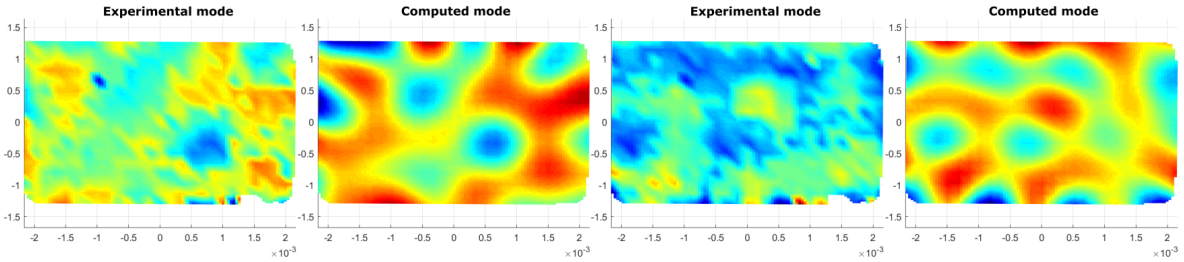

(g) Ti15Mo_V mode no. 93 ($\Delta f = 2{,}709$ kHz)

(h) Ti15Mo_V mode no. 97 ($\Delta f = 0{,}71$ kHz)

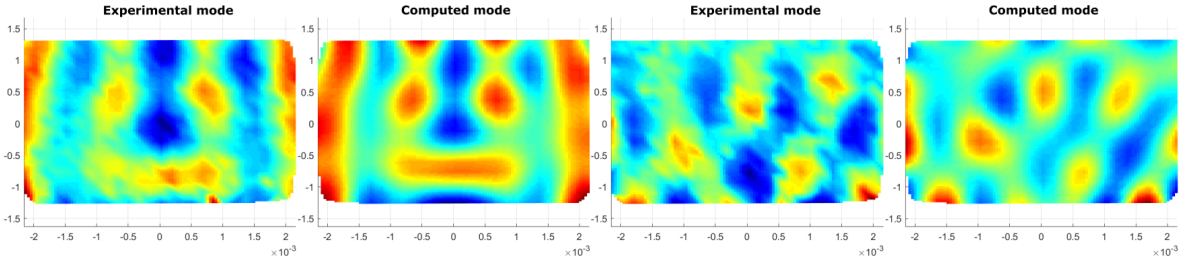

(i) Ti15Mo_W mode no. 116 ($\Delta f = 0{,}25$ kHz)

(j) Ti15Mo_W mode no. 118 ($\Delta f = 1{,}14$ kHz)

Figure 27: Selected matched modal shapes of the Ti15Mo alloy samples after generalized inversion

Again, to compare the differences between cubic optimization and full triclinic inversion, we have plotted cut of the Young's modulus in the direction of uniaxial load (plane (110)) in polar coordinates. Results are shown in Figure 28. Blue line represents Young's modulus calculated from cubic optimization results, while dashed orange line represents Young's modulus calculated from results of the triclinic inversion. Similar to LCB alloy, all of the samples have managed to retain their former cubic symmetry after the phase transition. Sample Ti15Mo_W, heat treated for 6 hours at 300°C and pressure 1000 MPa shows the biggest deviation of the Young's modulus, while all of the other samples remaining fully cubic. Unexpectedly, Sample Ti15Mo_V which underwent same heat treatment as the sample Ti15Mo_W, with exception of pressure of 800 MPa, shows practically no deviation from its former cubic symmetry. It means that the additional 200 MPa of pressure during the heat treatment caused more anisotropic precipitation of the secondary phase particles. A more detailed description of this problem will be part of the future research during doctoral studies.

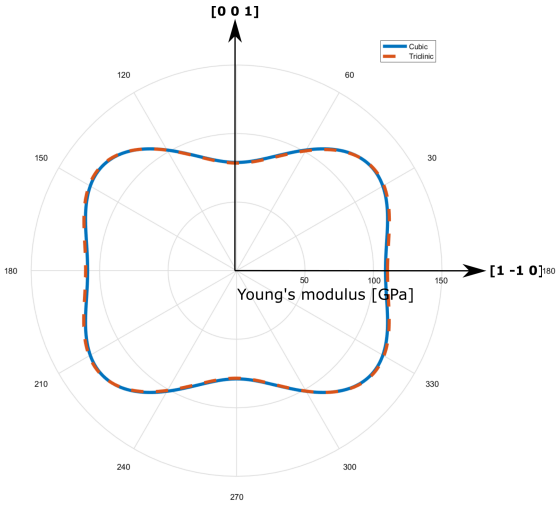

(a) Ti15Mo_AB_tc750

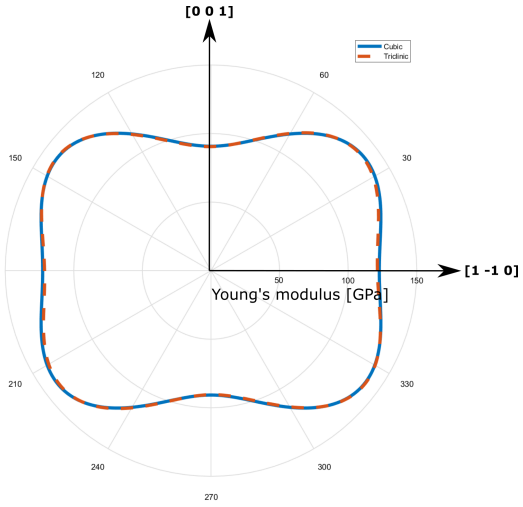

(b) Ti15Mo_L

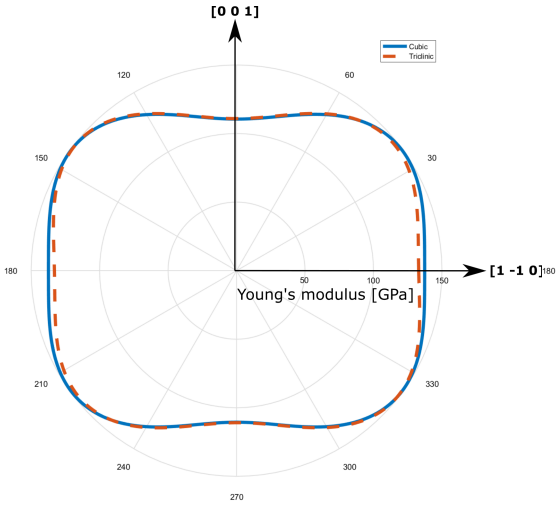

(c) Ti15Mo_R_po400

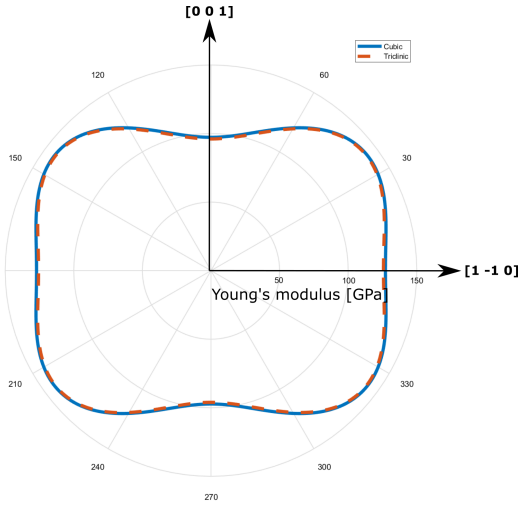

(d) Ti15Mo_V

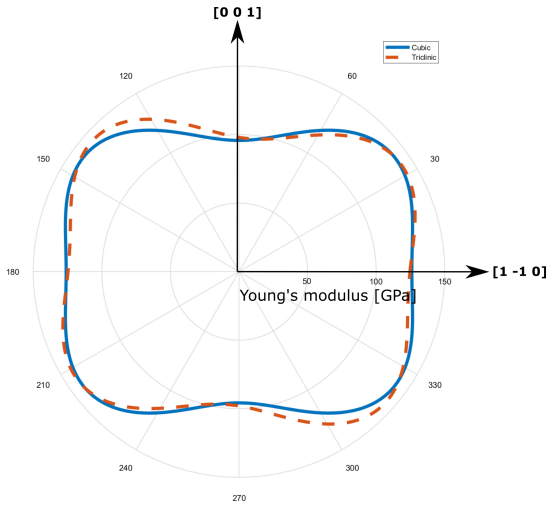

(e) Ti15Mo_W

Figure 28: (110)-cuts of Young's modulus surfaces for the optimal cubic (solid line) and triclinic (dashed line) fits

6 Summary

The main aim of this thesis was to test the reliability and precision of our extension of the inverse procedure which, in addition of calculating elastic coefficients with high accuracy, allows us to precisely refine the crystallographic orientations and dimension of the studied material. Tests were at first performed on synthetic data containing small perturbations in crystallographic orientations and dimensions, and later on 3 differently oriented samples of silicon-doped Fe single crystals. Our algorithm was then applied on 9 samples of metastable beta-Ti alloys, which contain particles of the low temperature coherent phase after heat treatment, to obtain information about a possible change of the material symmetry during phase transformation.

We summarize our most important results:

- All of the tests performed on synthetic data were successful. Two chosen examples fully represents the performance of the optimization procedure for all synthetic datasets. Results of these tests show the ability of our cubic optimization procedure to accurately refine the crystallographic orientations and dimensions used in inverse calculations to their real values.

- Tests performed on experimental data of 3 differently oriented single crystals of FeSi alloy resulted in successful refinement of the crystallographic orientation and dimension and in accurate determination of the elastic coefficient for each sample. Results of crystallographic orientations of the samples obtained from our cubic optimization procedure were compared with the results from Laue experiment. Our procedure shows same, if not even better accuracy in the determination of the crystallographic orientation of the material than the Laue method. We have also shown the significant difference in modal shapes and calculated resonant frequencies when our shape and orientation optimization is not utilized, but instead fixed orientation is assumed and classical approach to the elastic coefficient calculations is used.

- Finally, we were able to show changes of the symmetry of the metastable β-Ti alloys after the phase transformation by comparing the results of our extended cubic optimization procedure and full triclinic inversion. The symmetry change of the material was represented by the difference in (110)-cuts of Young's modulus surfaces between optimal cubic and triclinic fits. One of the samples, heated to 300°C under the pressure of 1000 MPa for 6 hours, shows deviations of its Young's modulus in the direction (111), while all of the other samples kept their former cubic symmetry after the phase transformation within the experimental error. It means that all of the other heat treatments produced more randomly oriented secondary phase precipitates which did not cause symmetry change of the material. This subject will be part of the follow-up research.

References

[1] J. Maynard. Resonant Ultrasound Spectroscopy. *Physics Today*, 49(1):26–31, 1996.

[2] J. L. Sarrao, S. R. Chen, W. M. Visscher, M. Lei, U. F. Kocks, and A. Migliori. Determination of the crystallographic orientation of a single crystal using resonant ultrasound spectroscopy. *Review of Scientific Instruments*, 65(6):2139–2140, 1994.

[3] M. Landa, P. Sedlák, H. Seiner, L. Heller, L. Bicanová, P. Šittner, and V. Novák. Modal resonant ultrasound spectroscopy for ferroelastics. *Applied Physics A*, (96):557–567, 2009.

[4] F. F. Balakirev, S. M. Ennaceur, and R. J. Migliori. Resonant ultrasound spectroscopy: The essential toolbox. *Review of Scientific Instruments*, 90(12):121401, 2019.

[5] R.B Schwarz and J.F Vuorinen. Resonant ultrasound spectroscopy: applications, current status and limitations. *Journal of Alloys and Compounds*, 310(1):243–250, 2000.

[6] P. Sedlák, H. Seiner, J. Zídek, M. Janovská, and M. Landa. Determination of All 21 Independent Elastic Coefficients of Generally Anisotropic Solids by Resonant Ultrasound Spectroscopy: Benchmark Examples. *Experimental Mechanics*, 54:1073–1085, 2014.

[7] A. Migliori, J.L. Sarrao, W. M. Visscher, T.M. B. Leisure, M. Lei, and Z. Fisk. Resonant ultrasound spectroscopic techniques for measurement of the elastic moduli of solids. *Physica B: Condensed Matter*, 183(1):1–24, 1993.

[8] Wikipedia. Resonant ultrasound spectroscopy, 2021.

[9] H. Seiner, L. Bodnárová, P. Sedlák, M. Janeček, O. Srba, R. Král, and M. Landa. Application of ultrasonic methods to determine elastic anisotropy of polycrystalline copper processed by equal-channel angular pressing. *Acta Materialia*, 58(1):235–247, 2010.

[10] J. Nejezchlebová. *Characterization of Microstructures in Titanium Beta-Alloys by Resonant Ultrasound Spectroscopy.* Phd thesis, Czech Technical University in Prague, 2019.

[11] H Ogi, K Sato, T Asada, and M Hirao. Complete mode identification for resonance ultrasound spectroscopy. *The Journal of the Acoustical Society of America*, 112(6):2553–2557, 2002.

[12] P. Sedlák, M. Janovská, L. Bodnárová, O. Heczko, and H. Seiner. Softening of Shear Elastic Coefficients in Shape Memory Alloys Near the Martensitic Transition: A Study by Laser-Based Resonant Ultrasound Spectroscopy. *Metals*, 10(10), 2020.

[13] J. Nejezchlebová, M. Janovská, P. Sedlák, J. Šmilauerová, J. Stráský, M. Janeček, and H. Seiner. Elastic constants of Beta-Ti15Mo. *Journal of Alloys and Compounds*, 792, 2019.

[14] H. Seo, D.-G. Song, and K.-Y. Jhang. Measurement of Elastic Constants by Simultaneously Sensing Longitudinal and Shear Waves as an Overlapped Signal. *Journal of the Korean Society for Nondestructive Testing*, 36:138–148, 2016.

[15] H. Seiner, J. Cizek, P. Sedlák, R. Huang, J. Cupera, I. Dlouhy, and M. Landa. Elastic moduli and elastic anisotropy of cold sprayed metallic coatings. *Surface and Coatings Technology*, 291:342–347, 2016.

[16] H.L. Alberts and P.T. Wedepohl. Elastic constants of dilute iron-silicon alloy single crystals below room temperature. *Physica*, 53(4):571–580, 1971.

[17] O. Kubasehewski. *Iron-Binary Phase Diagrams.* Springer, Berlin, 1 edition, 1982.

[18] Ch. Kloc, E. Arushanov, M. Wendl, H. Hohl, U. Malang, and E. Bucher. Preparation and properties of FeSi, α-FeSi2 and β-FeSi2 single crystals. *Journal of Alloys and Compounds*, 219(1):93–96, 1995.

[19] P.V. Geld, A.G. Volkov, S.V. Kortov, A.A. Pvzner, and V. Yu. Lvanov. Dokl. Akad. Nauk SSSR. 320:1097, 1991.

[20] J. Šmilauerová. *Phase transformations and microstructure changes inTIMET LCB alloy.* PhD thesis, Charles University in Prague, Faculty of Mathematics and Physics, 2012.

[21] P. Zhánal. *Study of Phase Transformations in Ti Alloys.* Master's thesis, Charles University in Prague, Faculty of Mathematics and Physics, 2014.

[22] D. De Fontaine. Simple models for the omega phase transformation. *Metallurgical Transactions A.*, 19(2):169–175, 1988.

[23] A. Terynková. *Metastable alloy Ti-15Mo prepared by powder metallurgy.* Master's thesis, Charles University in Prague, Faculty of Mathematics and Physics, 2019.

[24] S.K. Sikka, Y.K. Vohra, and R. Chidambaram. Omega phase in materials. *Progress in Materials Science*, 27(3):245, 1982.

[25] R. Bolmaro, V. Sordi, M. Ferrante, H. G. Brokmeier, M. Kawasaki, and T. Langdon. High-Pressure Torsion of Ti: Synchrotron characterization of phase volume fraction and domain sizes. *IOP Conference Series: Materials Science and Engineering*, 63:012147, 2014.

[26] M. Tane, Y. Okuda, Y. Todaka, H. Ogi, and A. Nagakubo. Elastic properties of single-crystalline ω phase in titanium. *Acta Materialia*, 61(20):7543 – 7554, 213.

[27] J. Nejezchlebová, M. Janovská, H. Seiner, P. Sedlák, M. Landa, J. Šmilauerová, J. Stráský, P. Harcuba, and M. Janeček. The effect of athermal and isothermal ω phase particles on elasticity of β-Ti single crystals. *Acta Materialia*, 110:185–191, 2016.

[28] J. Šmilauerová, P. Harcuba, J. Pospíšil, Z. Matěj, and V. Holy. Growth of ω inclusions in Ti alloys: An X-ray diffraction study. *Acta Materialia*, 61:6635–6645, 2013.

[29] P. Stoklasová, T. Grabec, K. Zoubková, P. Sedlák, S. Krátký, and H. Seiner. Laser-Ultrasonic Characterization of Strongly Anisotropic Materials by Transient Grating Spectroscopy. *Experimental Mechanics*, 61:1–14, 2021.